The Evolution of Hail Production in Simulated Supercell Storms

MATTHEW R. KUMJIAN,[a] KELLY LOMBARDO,[a] AND SCOTT LOEFFLER[a]

[a] *Department of Meteorology and Atmospheric Science, The Pennsylvania State University, University Park, Pennsylvania*

(Manuscript received 2 February 2021, in final form 25 June 2021)

ABSTRACT: Hailstorms pose a significant socioeconomic risk, necessitating detailed assessments of how the hail threat changes throughout their lifetimes. Hail production involves the favorable juxtaposition of ingredients, but how storm evolution affects these ingredients is unknown, limiting understanding of how hail production evolves. Unfortunately, neither surface hail reports nor radar-based swath estimates have adequate resolution or details needed to assess evolving hail production. Instead, we use a novel approach of coupling a detailed hail trajectory model to idealized convective storm simulations to better understand storm evolution's influence on hail production. Hail production varies substantially throughout storms' mature phases: maximum sizes vary by a factor of 2 and the concentration of severe hail by more than fivefold during 45–60-min periods. This variability arises from changes in updraft properties, which come from (i) changes in low-level convergence and (ii) internal storm dynamics, including anticyclonic vortex shedding/storm splitting, and the response of the updraft's airflow and supercooled liquid water content to these events. Hodograph shape strongly affects such behaviors. Straighter hodographs lead to more prolific hail production through wider updrafts and weaker mesocyclones and a periodicity in hail size metrics associated with anticyclonic vortex shedding and/or storm splitting. In contrast, a curved hodograph (favorable for tornadoes) led to a storm with a stronger but more compact updraft, which occasionally produced giant (10-cm) hail but that was a less-prolific severe hail producer overall. Unless storms are adequately sampled throughout their life cycles, snapshots from ground reports will insufficiently resolve the true nature of hail production.

KEYWORDS: Hail; Severe storms; Supercells

1. Introduction

Around the world each year, hailstorms rain damage and destruction on property and agriculture. Characterizing the hail threat from a given storm *throughout its lifetime* is important given the large socioeconomic impacts of hailstorms globally (e.g., Changnon et al. 2009; Brown et al. 2015; Punge and Kunz 2016; Púčik et al. 2019; Allen et al. 2020). Such information is directly relevant to operational severe weather warnings. For example, given the current hail threat, does it persist? Or does the threat wax and wane with storm evolution? Understanding the hail threat's spatiotemporal variability also could translate into improved risk models or assessments (e.g., Grieser and Hill 2019). Identifying when and where a given storm produced the largest and/or most damaging hail, if such information was available, also would be beneficial to insurance claims adjusters (e.g., Brown et al. 2015).

A storm's propensity for producing damaging hail is governed by the availability, placement, and timing of the ingredients necessary for hail. These ingredients include a sufficiently strong updraft capable of supporting growing hailstone pathways through the mixed-phase region of the storm, plentiful supercooled liquid drops, a source region for particles with sizes on the order of millimeters, which are often referred to as ''embryos'' and serve as the nucleus for growth, and airflow patterns that promote increased residence time within the storm's mixed-phase region. These ingredients are the product of the complex web of dynamic and microphysical processes ongoing in a storm, as well as the environment in which the storm is supported. Notably, supercell storms are known for their propensity to produce large hail (e.g., Nelson 1983; Miller et al. 1988; Tessendorf et al. 2005; Blair et al. 2011, 2017; Kumjian and Lombardo 2020, hereafter KL2020) owing to the favorable juxtaposition of ingredients found in such storms.

The AMS Glossary defines supercell storms as having ''quasi-steady'' updrafts. Indeed, storm steadiness has been assumed in prior hail trajectory or supercell hailstorm modeling studies (Nelson 1983; Ziegler et al. 1983; Miller et al. 1988; Grant and van den Heever 2014; Dennis and Kumjian 2017, hereafter DK17; KL2020). In a recent study employing a large ensemble of high-resolution tornadic supercell simulations, Markowski (2020) remarked that the simulated supercells ''are nearly steady throughout the simulations and would probably last forever if the simulations ran as long.'' Thus, a working hypothesis may be that, given the steadiness of supercell updrafts, presumably the ingredients modulating the growth and number of hailstones in supercell storms is also quasi steady.

However, any changes to these ingredients should, in principle, lead to variations in hail production. Such changes may arise from external heterogeneities, including terrain features and environmental thermodynamic or kinematic variations. Such heterogeneities are known to affect the environments of convective storms (e.g., Katona et al. 2016; Soderholm et al. 2017; Mulholland et al. 2020; Katona and Markowski 2021), which directly translates into changes in storm behavior, evolution, and associated hazards (e.g., Richardson et al. 2007; Markowski and Dotzek 2011; Lombardo and Kading 2018; Lombardo 2020; Letkewicz and Parker 2011). Even in homogeneous environments, however, storms evolve in ways that could lead to variations in hail ingredients. For example,

Corresponding author: Matthew R. Kumjian, kumjian@psu.edu

DOI: 10.1175/JAS-D-21-0034.1

© 2021 American Meteorological Society. For information regarding reuse of this content and general copyright information, consult the AMS Copyright Policy (www.ametsoc.org/PUBSReuseLicenses).

Brought to you by Pennsylvania State University, Paterno Library | Unauthenticated | Downloaded 10/11/21 01:54 PM UTC

supercell storms are known to sometimes exhibit a cycling behavior, as found in numerical simulations (e.g., Adlerman and Davies-Jones 1999; Adlerman and Droegemeier 2002, 2005) and observations (Beck et al. 2006; French et al. 2008; Kumjian et al. 2010). How does such cycling affect hail production?

Unfortunately, detailed observations of hailfall along supercell hail swaths are lacking. Some studies have provided clues into the finescale detail of hail swaths for very limited spatial regions (e.g., Morgan and Towery 1975; Changnon et al. 2009), but often these do not provide information on hail threat evolution *along* the swath. Some high-impact events have produced enough reports for National Weather Service poststorm analyses (e.g., National Weather Service 2016), but this is rare; most hailstorms only have a small number of reports (e.g., Allen and Tippett 2015; Blair et al. 2017). Research projects such as the Severe Hazards Analysis and Verification Experiment (SHAVE; Ortega et al. 2009) have provided high-resolution hail reports for storms. These data demonstrate considerable variability in hail size across the swath, but such well-characterized cases are limited in number. Thus, it is difficult to use such limited data to draw generalizations.

In contrast to direct hailstone measurements or reports, radar remote sensing offers an attractive solution to determine hail attributes over the life cycle of storms. Despite the development of numerous algorithms designed to estimate hail size (e.g., Aydin et al. 1986; Witt et al. 1998; Depue et al. 2007; Ryzhkov et al. 2013), however, radar hail sizing remains highly uncertain (Ortega et al. 2016; Witt and Snyder 2018; Murillo and Homeyer 2019; Allen et al. 2020; Brook et al. 2021). Additionally, it is unclear if the 4–5-min volume scan update times typical of operational radar scanning strategies are sufficient to capture any signals of variability in hail production.

As an alternate approach, one may employ numerical models coupled with detailed treatment of hail growth processes (e.g., Adams-Selin and Ziegler 2016; DK17; KL2020). Though these models have their own limitations, they do have advantages, including the ability to resolve sufficient details and information about the storm's microphysical and kinematic fields for process-level understanding, and the ability to control storm environments for sensitivity experiments. We opt for this approach in the present study.

The main goal of this work is to better understand how hail production varies in time for a given storm, and what in-storm processes lead to such variability. To do so, we employ idealized numerical modeling of supercell storms, coupled with our detailed hail growth trajectory model (KL2020).

2. Methods

For this study, we present the results of three idealized supercell simulations. The initialized environments and storms themselves will be described in the next section, but the storm-relative hodographs are provided in Fig. 1 for convenience. All three supercell storms are simulated in an idealized framework using Cloud Model 1 (CM1; Bryan and Fritsch 2002). The simulation design follows our previous work (DK17; KL2020); details may be found there. Briefly, the simulations employ the

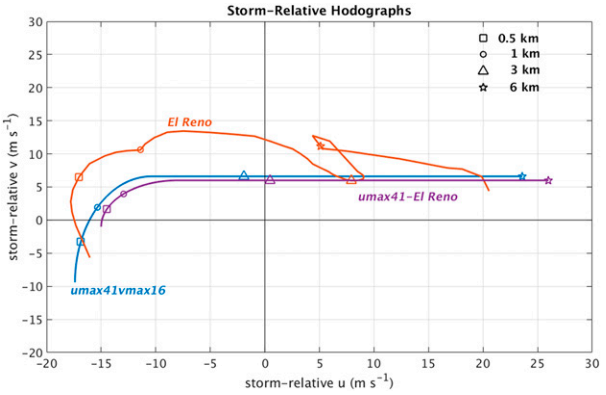

FIG. 1. Storm-relative 0–10-km hodographs used to initialize the three simulations herein. The blue, orange, and purple lines represent the umax41vmax16, El Reno, and umax41-El Reno cases, respectively. The markers indicate heights AGL: the square is 0.5 km, the circle is 1 km, the triangle is 3 km, and the pentagram is 6 km.

Morrison two-moment microphysics scheme (Morrison et al. 2009), no surface fluxes, no Coriolis, no PBL scheme, free-slip lower and upper boundary conditions, open-radiative lateral boundary conditions, and a Rayleigh sponge layer applied to the upper 5 km of the domain. We use the Klemp and Wilhelmson (1978) vertically implicit time-splitting pressure solver with the larger time step of 3 s. Subgrid-scale turbulence is parameterized with the Deardorff (1980) TKE scheme. The storms are initiated using a warm bubble (as in the standard CM1 package supercell simulation). The 120 km × 120 km × 20 km domain is translated with storm motion. Two of the simulations have 500-m horizontal grid spacing, and 250-m vertical grid spacing, with model output stored every 60 s. The third simulation has 1-km horizontal grid spacing and 500-m vertical grid spacing; the coarser resolution was needed to store a large number of output files for this case for use in the 4D trajectories described below. The output files for this coarser-grid-spacing simulation are stored every 30 s. Though the quantitative details of individual trajectories can vary between different grid spacings, the bulk statistics for the large numbers of trajectories used here are insensitive to grid spacing. Further, the statistics agree well with higher-resolution simulations of this storm from our previous work (DK17; KL2020). For example, the median, 90th-percentile, 95th-percentile, and 99th-percentile sizes[1] for the coarser-grid-spacing simulation on average are 7.87%, 10.75%, 9.29%, and 5.83% smaller than the finer-grid-spacing simulation used in KL2020. In contrast, the maximum size simulated is, on average, 25% smaller. The somewhat larger hail sizes in the finer-resolution simulation are explained by the larger number of embryo seeding locations, which can potentially open up more optimal pathways for growth. In addition, although the mean and 95th-percentile updraft speeds[2] are comparable in and below the hail growth region in both simulations, the

[1] Conditionally sampled for hailstone sizes ≥ 15 mm, as in KL2020.
[2] Conditionally sampled for $w \geq 15$ m s^{-1}.

Brought to you by Pennsylvania State University, Paterno Library | Unauthenticated | Downloaded 10/11/21 01:54 PM UTC

updraft area is up to twice as large in the coarser simulation presented here, in line with expectations based on Lebo and Morrison (2015) and others.

We use the hailstone growth trajectory model of KL2020. Briefly, initial hailstone embryos are seeded at specified locations throughout the domain of the CM1 simulation output. These embryos are then advected by the CM1 simulation's three-dimensional wind field. Detailed microphysical processes governing hail growth are calculated explicitly using the CM1-simulated hydrometeor and thermodynamic fields at each grid box. The growth of high-density particles by riming in the bulk microphysics scheme used in CM1 will deplete supercooled liquid cloud droplets from regions of the storm's updraft. Therefore, hail growth from our trajectory model launched at a given model output time could encounter this already-depleted liquid water content. Because our trajectory model is run offline and does not affect the CM1 storm simulation, however, we believe this approach is a practical way to account for the effects of prior hail growth on the storm's structure. If the supercooled liquid water was not depleted in the simulated storm, hail growth in our trajectory calculations may be overestimated. Thermal energy balance equations are solved to determine the hailstone growth regime (i.e., wet vs dry). The hailstones grow until they fall out of the storm or are advected out of the domain. Melting of hailstones is not considered. The trajectory model produced plausibly realistic hailstone sizes and fallout locations, at least for an idealized squall line and supercells, as shown in KL2020. Further details and sensitivity tests are found in that study.

For the trajectory calculations here, we extract a subset of the simulation domain comprising a 50 km × 50 km region centered on the maximum updraft speed at 6 km AGL. Initial embryo diameters used are 2.5, 5.0, 7.5, and 10.0 mm, each with an initial density equal to that of solid ice, which approximates frozen raindrop embryos (e.g., Knight 1981). See KL2020 for sensitivities of the trajectory calculations to embryo size and density choices. For the two higher-resolution simulations, each of the four embryo sizes are seeded one per grid box in a cube defined by $x = -15.5$ km to $x = 9.5$ km, $y = -13.0$ to $y = 12.0$ km, and $z = 2.375$ to $z = 11.125$ km AGL, encompassing the updraft and surrounding regions. These heights correspond to temperatures between about 9° and −47°C, and were chosen to cover reasonable heights at which the embryos might enter the updraft (e.g., Adams-Selin and Ziegler 2016). Such embryo seeding produces 374 544 trajectories for each model output time. For the coarser-resolution simulation, the embryos similarly are seeded one per grid box in a cube defined by $x = -25.5$ km to $x = 24.5$ km, $y = -25.5$ km to $y = 24.5$ km, and $z = 3.25$ km to $z = 11.25$ km AGL (corresponding to temperatures between about 1° and −49°C), resulting in 176 868 trajectories for each output time used.

To explore how hail production changes during a storm's life cycle, we can take two approaches with the trajectory model. The first is to run trajectories through an evolving storm by seeding at some initial time, and allowing the CM1 fields to update at each model output time without reinitializing embryos. We call these calculations "4D trajectories." The second is to seed a new set of embryos at each CM1 model output time, and compute the full trajectory lifetime (typically ≤20 min; KL2020) without updating the model fields, assuming they are steady state. This is repeated for each model output time independently, and bulk statistics for each set of trajectory calculations are stitched together to reveal the full evolution of hail production during the storm's lifetime. We refer to this as the "steady-state fields" approach, which computationally is more feasible and highly parallelizable for us when running very large numbers of trajectories. As such, we mainly focus on the steady-state fields approach here. However, we also demonstrate that results are qualitatively similar when running 4D trajectories versus steady-state fields.

3. Results and analysis

a. *The umax41vmax16 supercell*

The first storm analyzed here has an environment characterized by the analytic thermodynamic sounding from Weisman and Klemp (1984), with 2200 J kg^{-1} of CAPE. The wind profile is specified by a quarter-circle hodograph (Weisman and Rotunno 2000) with maximum ground-relative zonal (u) wind speed of 41 m s^{-1} at 6 km AGL and maximum ground-relative meridional (v) speed of 16 m s^{-1} at 2 km AGL, which was called the "umax41vmax16" simulation in DK17 (see their Figs. 1 and 11) and KL2020. We will adopt this terminology, too. The storm-relative hodograph for this case is shown in Fig. 1 (blue line). The mixed-phase region of the updraft resides between about 4 km AGL (~0°C) and 10.9 km AGL (~−40°C).

The analysis is performed for an arbitrarily chosen 45-min period during the storm's mature phase, from 135 to 180 min into the simulation, using the "steady-state fields" approach. This is the coarser simulation for which output files are stored every 30 s. As in KL2020, we conditionally sampled final hailstone sizes for those reaching ≥15 mm; hail size metrics as a function of output time are shown in Fig. 2. Larger hail sizes at a given time indicate that the storm structures *at that time* are favorable for hail production, even though in reality the storm will evolve and hail may reach the surface sometime later. Despite only subtle changes to the median size, the maximum sizes vary over the 45-min period, from a minimum of about 4.0 cm to a maximum of almost 6.5 cm. That the maximum diameters are always >4 cm for this supercell is consistent generally with observations reported by Blair et al. (2017), which suggest Great Plains supercells nearly always produce >3.8-cm hail. The 90th-, 95th-, and 99th-percentile sizes feature similar evolution to the maximum size, though over a smaller range. The number of seeds resulting in severe-sized hail (Fig. 2b) generally increases throughout the simulation, nearly tripling by the end of it. These changes occur exclusively because of changes to storm structure and airflow patterns, as the base-state environment is homogeneous and steady throughout the simulation. Thus, this simulation demonstrates that *hail production can change throughout a storm's mature phase despite static antecedent environmental conditions.*

To understand the causes of the fluctuations in hail production, we examined the final distributions of hail sizes resulting from all initial embryo seeds for each time (Fig. 3). We subjectively separated the size distributions into categories representing large-hail production times (colored in blue; $n = 24$), smaller-hail production times (colored in gray; $n = 56$), and the minimum hail production times (colored in black; $n = 12$), based on visual

Brought to you by Pennsylvania State University, Paterno Library | Unauthenticated | Downloaded 10/11/21 01:54 PM UTC

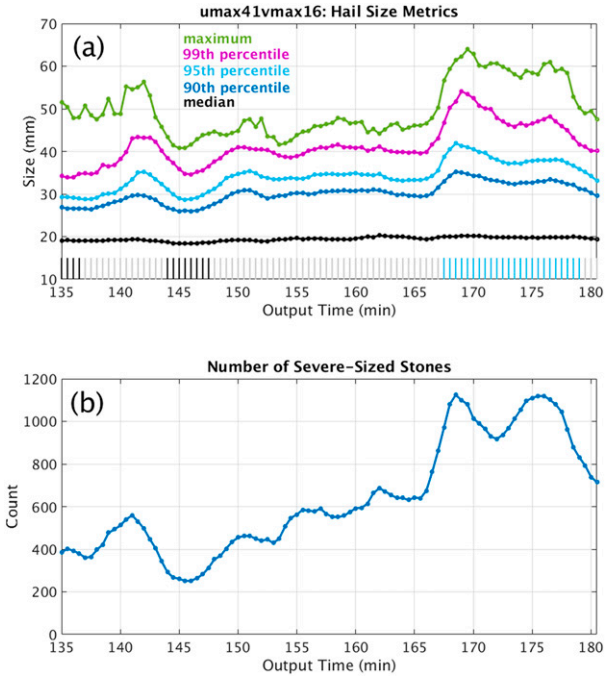

FIG. 2. Results from the umax41vmax16 simulation using the "steady-state" approach, showing time series of (a) hail size metrics conditionally sampled for hailstones with final sizes ≥ 1.5 cm, including maximum size (green), 99th-percentile size (magenta), 95th-percentile size (cyan), 90th-percentile size (blue), and median size (black) and (b) number of initial seeds that resulted in final sizes exceeding the severe threshold (>2.54 cm). These statistics are calculated independently for embryos initialized at each 30-s model output time and then stitched together into this time series. The vertical bars at the bottom of (a) are the subjectively identified periods of smallest-hail times (black), small-hail times (gray), and large-hail times (blue); see text for details.

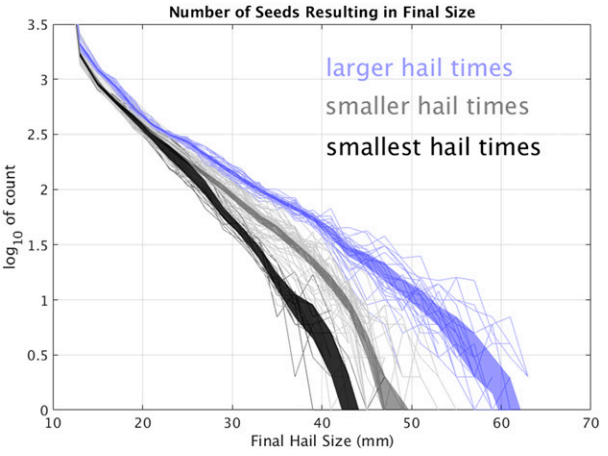

FIG. 3. Distribution of the number of initial embryo seeds becoming hailstones of a given final size. The individual distributions (lines) are manually color-coded such that blue indicates "larger-hail" times, gray the "smaller-hail" times, and black the "smallest-hail" times. The shaded bands indicate the bootstrapped 95% confidence interval about the mean values in each size bin, color-coded for each group.

inspection of the ≥35–40-mm portion of the size distributions in Fig. 3. These color-codings are reproduced as vertical bars on the bottom of Fig. 2a, and show good agreement with the hail metrics. The minimum hail-production times correspond to <400 severe-sized hailstones, and 90th-, 95th-, and 99th-percentile sizes below roughly 2.8, 3.0, and 3.6 cm, respectively. In contrast, the maximum hail-production times correspond to >900 severe-sized hailstones, and 90th-, 95th-, and 99th-percentile sizes above about 3.1, 3.5, and 4.2 cm, respectively. Within each of these subjectively identified categories, we applied a bias-corrected-and-accelerated bootstrapping technique (e.g., Efron and Tibshirani 1993) with 1000 samples in each 0.2-mm-wide bin of the size distribution to estimate the 95% confidence interval about the mean count; these are shown in Fig. 3 as shaded bands. The confidence intervals for each category are separated for sizes >2.5 cm, indicating that, despite subjectively classifying the time periods by visual inspection, the resulting categories do exhibit statistically significantly different amounts of hail of a given size exceeding the severe threshold.

We then applied the same classifications to the mean vertical profiles of cloud liquid water mass mixing ratio (q_c) within the updraft, defined here as $w \geq 15\,\mathrm{m\,s^{-1}}$. The resulting 95% confidence intervals about the means for each category are shown in Fig. 4, and reveal that the times of greater hail production are associated with statistically significantly larger mean q_c values below 7 km AGL (i.e., at temperatures > −16°C). This makes sense: all else being equal, larger amounts of supercooled liquid water in the hail growth region would result in larger growth rates, and thus larger final hail sizes. The confidence intervals about the mean q_c for periods of smaller and minimal hail production (gray and black, respectively) are overlapped, indicating no meaningful differences.

Is this the whole story? Though a critical ingredient for hail production, growth rates can only be achieved if hailstones actually spend time in the updraft's hail growth zone. Using the same identified time periods applied to the distribution of hailstone residence times within the $w \geq 15\,\mathrm{m\,s^{-1}}$ updraft (Fig. 5) shows a clear distinction between longer residence times in the updraft (blue) for the periods of enhanced hail production, and smaller residence times for the other periods. Table 1 shows different quantiles of these residence times for the three identified time periods. These residence times are consistent with those found in previous studies (e.g., Nelson 1983; Adams-Selin and Ziegler 2016; KL2020). Again, this agrees with physical intuition. Growing hailstones that spend less time in the updraft and hail growth zone would achieve smaller sizes, and overall fewer trajectories taking long paths through the updraft result in fewer large hailstones.

Differing residence times suggest the airflow patterns may be changing throughout the storm evolution (e.g., KL2020). To understand why the residence times differ, we explore storm structural features that may change between the different hail-production periods. We see that, perhaps surprisingly, during the times associated with larger hail, the storm has *weaker* updrafts on average throughout a large depth of the storm, indicated by both the 1–3 $\mathrm{m\,s^{-1}}$ smaller mean w and 3–5 $\mathrm{m\,s^{-1}}$ smaller 95th-percentile w (hereafter $w_{95\%}$) values, both

Brought to you by Pennsylvania State University, Paterno Library | Unauthenticated | Downloaded 10/11/21 01:54 PM UTC

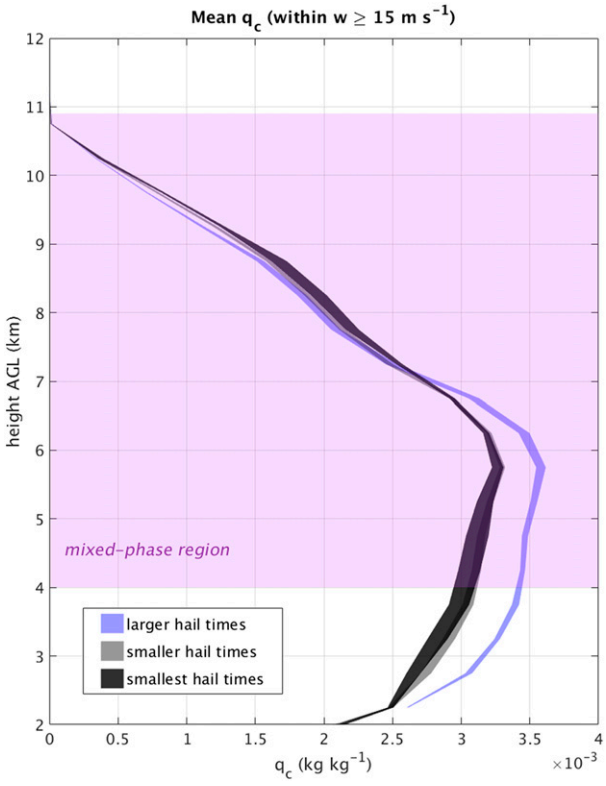

FIG. 4. The 95% confidence intervals about the average cloud droplet mass mixing ratio q_c within the 15 m s^{-1} updraft as a function of height. The color-codings are as in Fig. 3. The pink region highlights the approximate in-updraft mixed-phase region (0° to −40°C).

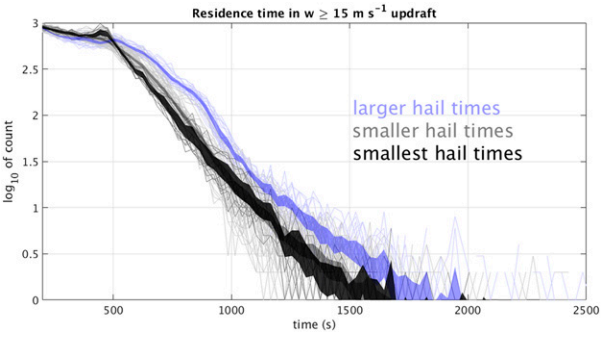

FIG. 5. Distributions of residence times within the 15 m s^{-1} updraft for hailstones, for calculations at each output time. Shaded bands show the 95% confidence interval about the mean values in each time bin, color-coded for each group. The color-codings are as in Figs. 3 and 4.

conditionally sampled for $w \geq 15$ m s^{-1} (Fig. 6a). As a corollary, during the times of the minimal hail production, the storm has *stronger* updrafts. Further, the times of greatest hail production correspond to significantly larger updraft areas throughout the entire hail growth region (Fig. 6b). This is in agreement with previous studies that found updraft breadth was important for hail production (e.g., Nelson 1983; DK17; KL2020). That the wider updrafts contain greater liquid water content (Fig. 4) is consistent with Peters et al. (2019, 2020), who found wider updrafts are better protected from the deleterious effects of entrainment of environmental dry air. These results also show that supercell updraft characteristics (strength, breadth) evolve quite markedly throughout the storm's life cycle.

To investigate the storm structures further, we conditionally sample the $u > 0$ (west-to-east) and $v > 0$ (south-to-north) components[3] of the storm-relative horizontal winds within the updraft ≥ 15 m s^{-1}. These components represent the "inflow-side" half of the mesocyclone or vortex segment (Dahl 2017) for supercell storms in this configuration, with a predominantly zonal deep-layer shear vector, and serve as a possible conduit for a favorable hail growth trajectory (e.g., KL2020). Whereas there are only small differences in the in-updraft $u > 0$ wind component at all heights (Fig. 7), the in-updraft $v > 0$ wind components show more substantial differences, including significantly weaker $v > 0$ flow in the lower part of the hail growth zone during the larger-hail times. This finding that a weaker southerly branch of the mesocyclone promotes larger residence times is consistent with the varying-shear simulations in KL2020. Figure 7 also shows significantly larger areas of updraft containing $u > 0$ and $v > 0$ horizontal flow at the large-hail times compared to the smaller-hail times. This implies that, within the overall updraft expansion during large-hail times, in particular, the portions of the updraft with favorable flow patterns for hail trajectories expand.

For this storm, the horizontal winds in the updraft's hail growth region mainly have a southerly component: the volume of $v < 0$ winds within the 15 m s^{-1} updraft is an order of magnitude smaller than the volume of $v > 0$ winds (not shown). As such, the $v < 0$ component is considered much less important for hail growth in this storm. In contrast, the volume of $u < 0$ (easterly) wind throughout the hail growth region is comparable to that of $u > 0$, and actually larger than that of $u > 0$ in lower portions of updraft, beneath the hail growth region. The mean $u < 0$ within the $w \geq 15$ m s^{-1} updraft also tends to be 1–2 m s^{-1} weaker during the large-hail times (not shown). Combining these findings, we can calculate the "favorable" horizontal wind speed, defined here as the horizontal wind speed where $v > 0$; conceptually, this corresponds to the wind speed of the right half of a closed mesocyclone in the Northern

TABLE 1. Quantiles of residence times (s) of hailstones within the 15 m s^{-1} updraft for each subjective growth category.

Hail growth category	10%	25%	50%	75%	90%	95%	99%
Large-hail times	49	129	299	520	695	808	1052
Small-hail times	50	128	275	458	612	708	934
Smallest-hail times	48	125	271	443	576	679	940

[3] The horizontal airflow within the updraft may be separated into any arbitrary orthogonal components. We select u and v because of their traditional meaning in meteorology, our previous work (KL2020), and for the mesocyclone structure common of Northern Hemisphere supercells. Note that more generally, we recommend using horizontal flow components parallel to and orthogonal to the deep-layer shear vector.

Brought to you by Pennsylvania State University, Paterno Library | Unauthenticated | Downloaded 10/11/21 01:54 PM UTC

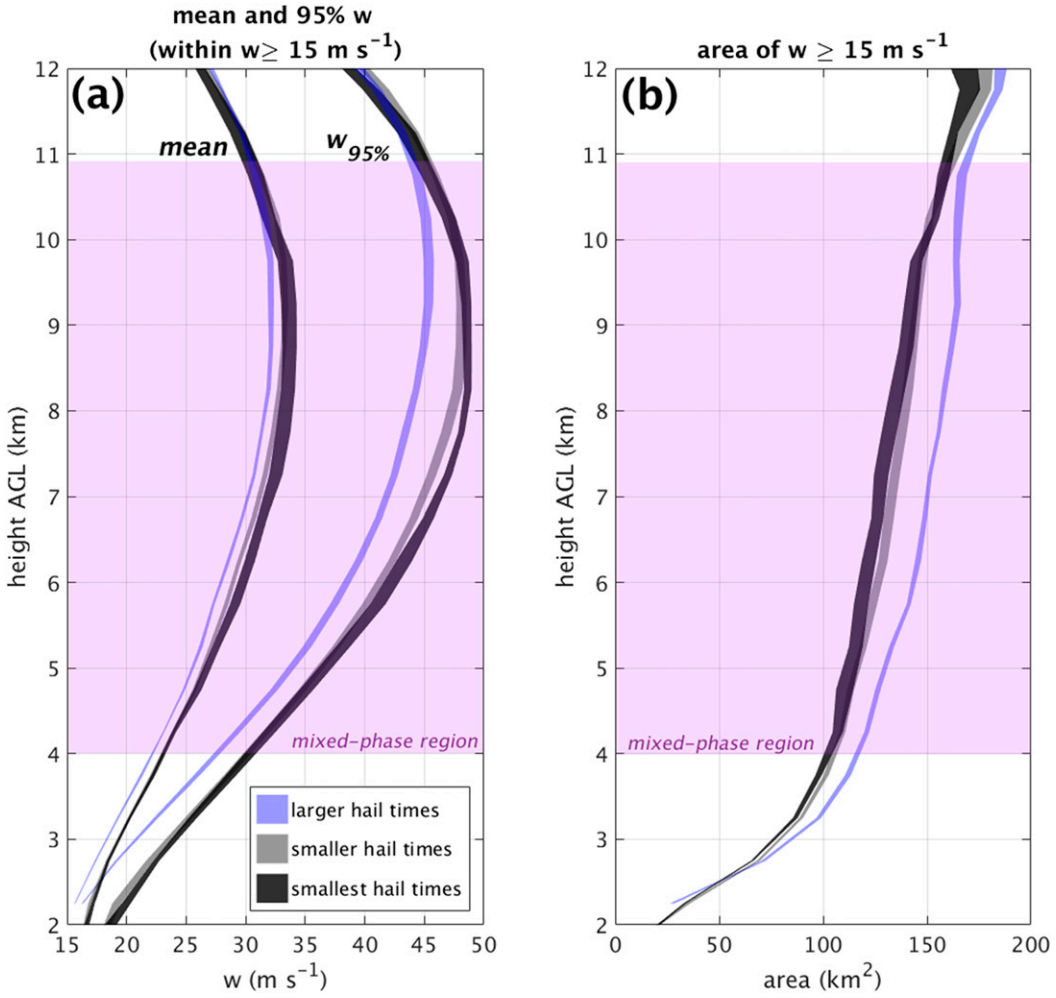

FIG. 6. (a) Vertical profiles of the 95% confidence intervals about the mean (left profile), and 95th-percentile (right profile) updraft speeds within the 15 m s^{-1} updraft for each output time, color-coded as before. (b) The 95% confidence interval about the mean updraft area at each level within the 15 m s^{-1} updraft. The pink regions highlight the approximate in-updraft mixed-phase region (0° to −40°C).

Hemisphere. This favorable horizontal wind speed shows smaller magnitudes at large-hail times and some of the largest magnitudes during the smallest-hail times below 9 km AGL (Fig. 8). That the confidence interval is narrower for large-hail times within and beneath the hail growth region may be a consequence of this particular storm's dynamics; in general, we would expect smaller values are more favorable for hail production, all else being equal. Though the difference in favorable wind speeds between large-hail times and the smallest-hail times is <5 m s^{-1} throughout much of the hail growth region, this difference becomes important for substantially increasing residence times as the hailstones are advected across the broad updraft with pathlengths of a few kilometers. For example, given a pathlength of 8 km within the updraft, a 4 m s^{-1} decrease in the advecting horizontal flow from 25 to 21 m s^{-1} increases residence time by a full minute.

Figure 9 is a "corner plot" that summarizes the relationships between various storm attributes, and between those attributes and hail production. Each dot represents one CM1 simulation output time and thus a set of trajectory calculations, and each row/column is a storm structural feature of interest conditionally sampled for within the $w \geq 15$ m s^{-1} updraft. For example, a strong negative correlation ($r < -0.8$) is observed between updraft intensity (both $w_{95\%}$ and the mean w) and the updraft area. Interestingly, despite weaker correlations, mean q_c shows a strongly nonlinear relationship with updraft area, increasing as wider updrafts are less susceptible to dilution (e.g., Peters et al. 2019). Further, the dot color is an indicator of large-hail production. Here we use the number of hailstones > 2.5 cm in diameter produced from the initial embryo seedings, but other metrics show similar results. Coloring by the number of severe-sized hailstones shows portions of the joint parameter spaces where storm attributes are favorable for hail production. In particular, favorable hail production occurs for weaker mean $u < 0$ regions, weaker mean $v > 0$ regions, larger mean q_c, smaller $w_{95\%}$, smaller mean w, larger w area, and

Brought to you by Pennsylvania State University, Paterno Library | Unauthenticated | Downloaded 10/11/21 01:54 PM UTC

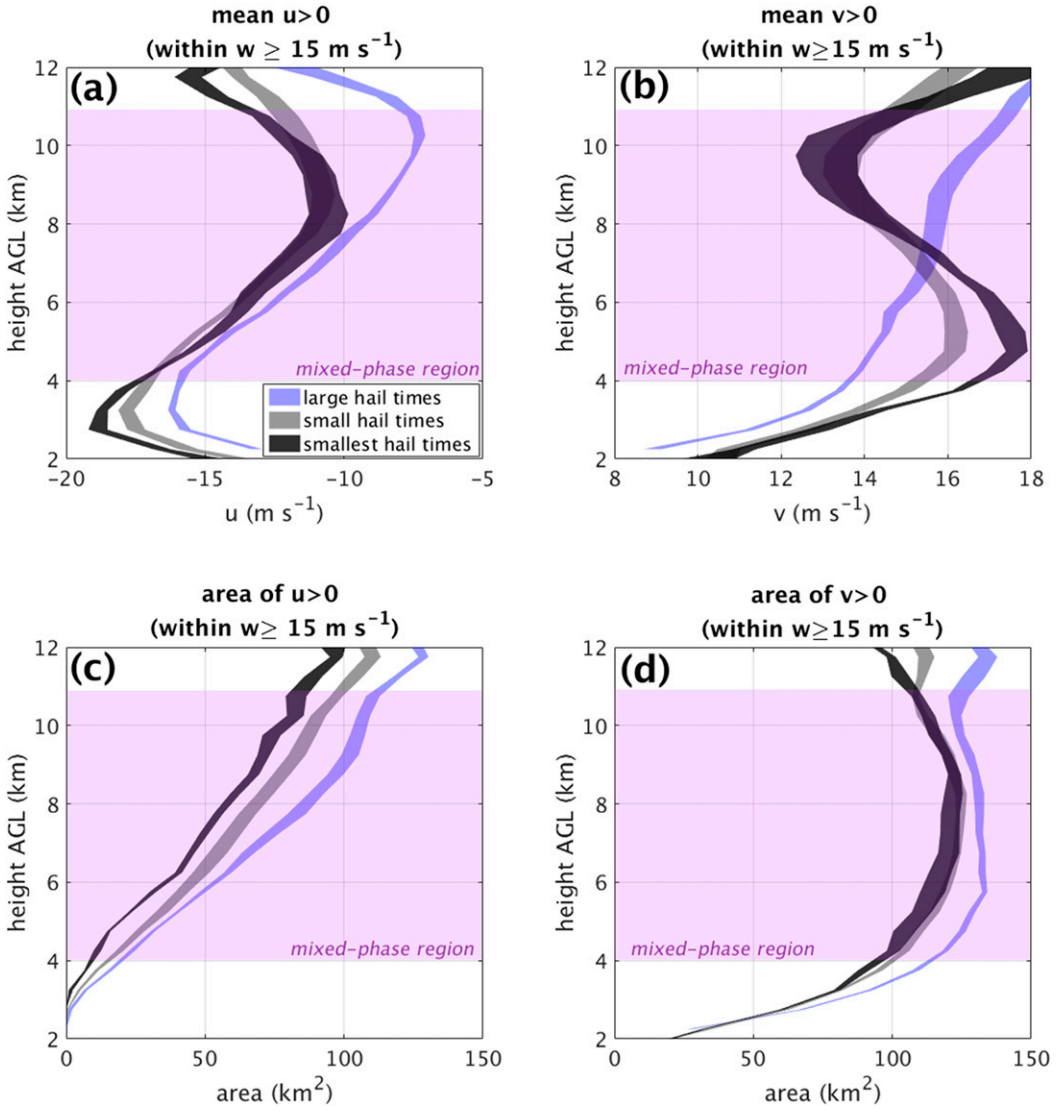

FIG. 7. The 95% confidence intervals about the (a) mean storm-relative $u > 0$ flow component within the 15 m s^{-1} updraft at each height and time and (b) the mean storm-relative $v > 0$ flow component. (c) Area of storm-relative $u > 0$ flow within the 15 m s^{-1} updraft and (d) area of storm-relative $v > 0$ flow within the 15 m s^{-1} updraft. The pink regions highlight the approximate in-updraft mixed-phase region (0° to −40°C).

smaller mean favorable horizontal speeds. Although the corner plot features relationships between storm properties and the number of severe-sized hailstones at 5.25 km AGL, similar strong correlations for mean w, $w_{95\%}$, w area, and mean favorable horizontal wind speed are also observed throughout the updraft mixed-phase region (not shown).

To better visualize the storm structural features at large- versus small-hail times, we construct composites based on a grid centered on the maximum w at 6 km AGL, following Grant and van den Heever (2014) and DK17. Figure 10 is a horizontal slice through the lower portion of the hail growth region at 5.25 km AGL, showing composited storm structures for large-hail times (168–170.5 min) and small-hail times (144–146.5 min), as well as the difference in composite fields. A notable difference in the midlevel updraft structure is evident on its northwest side, where the larger-hail-times composite features an expanded region of strong updraft, though note the updraft also has a weakened core. Some expansion of the updraft on south side is also evident during large-hail times. Across the eastern half of the updraft, the composite difference horizontal wind vectors point southward. Given the storm-relative southerly flow in this region at both composite times, such difference vectors imply weaker southerly flow in this branch of the mesocyclone during the large-hail times. Another notable feature in the difference fields is the cyclonic vortex on the northwest portion of the updraft. This is a result of an anticyclonic vortex during the small-hail times that has moved away to the north-northwest by the large-hail times.

Brought to you by Pennsylvania State University, Paterno Library | Unauthenticated | Downloaded 10/11/21 01:54 PM UTC

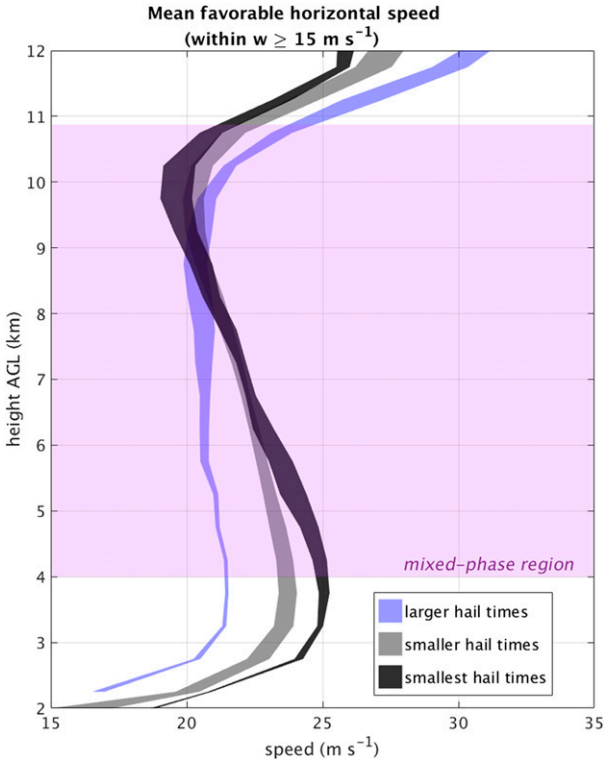

FIG. 8. Average horizontal "favorable" wind speed within the 15 m s^{-1} updraft (i.e., wind speed magnitude for any region of the updraft with a storm-relative $v > 0$ wind component) at all heights, color-coded as in previous figures. The pink region highlights the approximate in-updraft mixed-phase region (0° to −40°C).

Interestingly, this advection of the anticyclonic vortex northward, which we will call vortex shedding, appears to be associated with the updraft expansion into that region. Environments with straighter hodographs, like that of the umax41vmax16 supercell, often contain a large crosswise component to the horizontal vorticity. Tilting of this crosswise horizontal vorticity into the vertical by the updraft leads to anticyclonic vertical vorticity on the left flank of the updraft, and promotes storm splitting (e.g., Davies-Jones et al. 2001; Markowski and Richardson 2010; Dahl 2017).

This simulation reveals changes in hail production arising owing to changes in the updraft structure and intensity. What drives these changes? Time–height depictions of various updraft intensity metrics (mean w, max w, $w_{95\%}$, etc.) reveal a decreasing trend over the analysis period, superposed with upward-propagating features that appear to originate at low levels. Also, the updraft area generally increases during this period (not shown). Combined, the times with weaker and wider updrafts provide more favorable conditions for severe hail production (cf. Fig. 9) and explain the tripling of the number of severe hailstones produced over the period. The upward-propagating structures appear with various updraft thresholds and metrics, though for illustrative purposes, Fig. 11a shows relative changes in $w_{95\%}$ conditionally sampled for $w \geq 5$ m s^{-1}, with the values computed using the time-averaged $w_{95\%}$ at each altitude for better visualization. To understand the origin of these upward-moving features, we focus our attention on the low-level forcing for ascent. We examine the mean convergence magnitude at the lowest model level, $\overline{|\delta_0 < 0|}$, conditionally sampled for values $>$ 0.005 s^{-1} (Fig. 11b). This value was chosen by manual inspection to encompass the region beneath the main updraft and along the rear-flank gust front of the simulated supercell, but not other regions in the cold pool, etc. This is compared to $w_{95\%}$ (conditionally sampled for $w \geq 5$ m s^{-1}) at the second-lowest model level, with the expectation—based on mass continuity—that low-level convergence strength and updraft intensity should be related. Indeed, the two time series are strongly correlated (r = 0.892) at 2-min lag. Figure 11b shows that the mean convergence magnitude also exhibits a decreasing trend in time over the 45-min analysis period; when the linear trends in $w_{95\%}$ and $\overline{|\delta_0 < 0|}$ are removed, the linear correlation is still strong (r = 0.731 at 1.5-min lag, not shown). Both of these correlations decrease with increasing lag time. Removing the linear trends focuses the correlation on small perturbations instead of the overall trends; the fact that both the raw time series and detrended time series of $w_{95\%}$ and $\overline{|\delta_0 < 0|}$ are strongly correlated indicates both the perturbations and longer-term trends of these two variables are related.

We can link these low-level changes in convergence strength to hail production aloft by taking the time-lagged linear relationships between hail size metrics and $\overline{|\delta_0 < 0|}$. Figure 12 shows the lagged linear correlation coefficient r_L between the detrended number of severe-sized hailstones[4] and the detrended $\overline{|\delta_0 < 0|}$. The physical interpretation of r_L here is that changes in low-level convergence characteristics lead changes in hail size metrics. The moderate negative correlations around 5.5 min (minimum r_L = 0.656) indicate that decreases in convergence strength (and thus decreases in low-level updraft strength) are correlated to increases in severe hail production 5.5 min later. Other hail size metrics reveal similar peaks in the r_L magnitude at these lag times (not shown). When using the original time series with the long-term trends, the correlation magnitude increases to r_L = 0.922 at 6-min lag time. Thus, both short-time-scale fluctuations and the long-term trends between low-level convergence strength and severe hail production are negatively correlated.

Do these temporal lags make sense? Using the time-averaged mean updraft speed (within $w \geq 7.5$ m s^{-1}) at each height level, it would take an air parcel on average 7.38 min (442.8 s) to ascend from 0.75 km (the first level where the mean is defined using this threshold) to 7.25 km, 6.75 min to 6.25 km, and 6.0 min to 5.25 km. Thus, the lagged correlations are perfectly consistent with low-level features propagating upward to where they impact hail production in the lower portion of the hail growth zone.

In addition to changes at low levels, storm internal dynamics can play a role in modulating updraft width and intensity. As seen in Fig. 10, the simulated storm produced anticyclonic vortices on its updraft's northwest flank, which subsequently

[4] According to Fig. 2b, the number of severe-sized hailstones also displays an increasing trend over the analysis period, so detrending is necessary to capture the shorter-time-scale perturbations.

Brought to you by Pennsylvania State University, Paterno Library | Unauthenticated | Downloaded 10/11/21 01:54 PM UTC

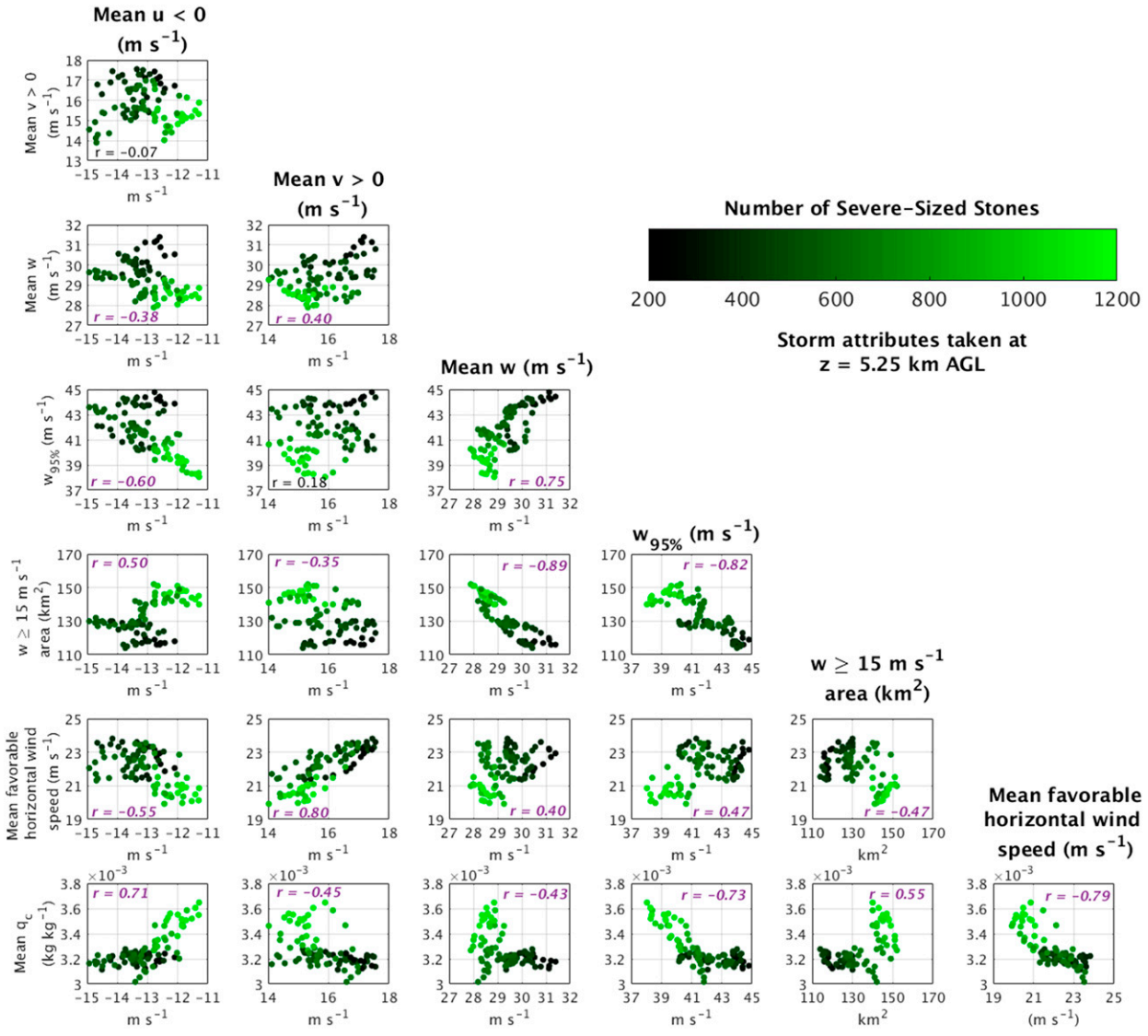

FIG. 9. "Corner plot" where each panel shows the correlations between important storm attributes (one dot for each output time). Storm attributes are listed at the top of each column and to the left of each row. The color of the dots represent the number of severe-sized hailstones (according to scale). The storm attributes are taken at 5.25 km AGL, within the lower portion of the hail growth zone. Each panel also contains the linear correlation coefficient r between storm attributes; those that are statistically significantly different from 0 at the 95% confidence level are italicized and in purple font.

moved off to the north. This behavior is typical of storms in environments with relatively straight hodographs (like the one used here), which tend to promote storm splitting (e.g., Markowski and Richardson 2010). This region of anticyclonic vorticity on the updraft's northwest flank is associated with an elevated negative nonlinear dynamic pressure perturbation (i.e., perturbation low pressure). This negative pressure perturbation sets up an upward vertical perturbation pressure-gradient acceleration on the flank of the updraft, and would promote expansion of the updraft on this flank. Additionally, the advection of w by the horizontal winds within the updraft and vertical advection of w (calculations not shown) may help the updraft expand. An increased updraft area is associated with a wider region of positive buoyancy, and therefore a greater magnitude of the downward-directed buoyancy pressure perturbation force above the buoyancy maximum. All else being equal, this results in weaker vertical velocities overall (e.g., Markowski and Richardson 2010; Morrison 2016).

In summary, analysis of the umax41vmax16 simulation reveals that perturbations to the low-level convergence strength (themselves likely arising owing to a complicated, nonlinear web of events including prior updraft intensity perturbations, precipitation production and fall out, and cold pool production), in conjunction with internal storm dynamics associated with shedding anticyclonic vortices and/or splitting, lead to fluctuations in the updraft breadth

Brought to you by Pennsylvania State University, Paterno Library | Unauthenticated | Downloaded 10/11/21 01:54 PM UTC

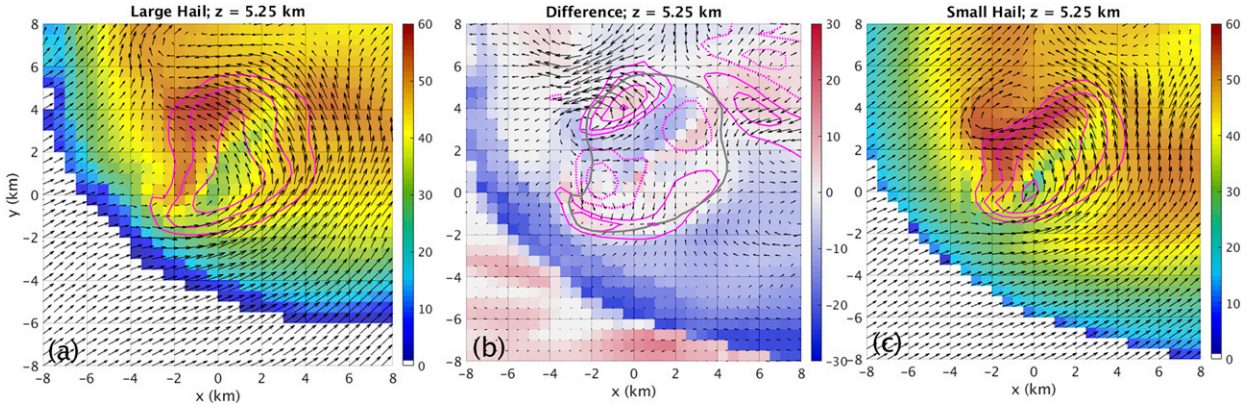

FIG. 10. Composite of (a) large-hail times (168–170.5 min) and (c) smallest-hail times (144–146.5 min). In each, simulated reflectivity factor is shown (shaded according to scale in dBZ), overlaid with contours of w (10, 20, 30, and 40 m s^{-1}, magenta lines) and horizontal storm-relative wind vectors (black arrows). (b) The difference in the composites (large minus small); w differences are in magenta contours (5, 10, 20, 30, and 40 m s^{-1}), with dashed for negative and solid for positive. The horizontal wind vectors (u,v, black) show the vector difference. The gray solid line in (b) represents the 10 m s^{-1} updraft contour from the large-hail-times composite, for reference.

and intensity in the hail growth region. These changes in updraft structure directly affect hail production, and are correlated to changes in hail sizes and the number of severe-sized hailstones.

b. *The 24 May 2011 El Reno supercell*

We next investigate an environment much more favorable for severe weather—that of the 24 May 2011 El Reno, Oklahoma, significantly tornadic supercell (e.g., see French et al. 2013, 2015; Orf et al. 2017). The environment (Fig. 1, orange line; Fig. 13) is characterized by large CAPE (4211 J kg^{-1}) and 0–6-km bulk wind difference (>25 m s^{-1}). The simulated supercell storm has intense updrafts, with $w_{95\%}$ at times exceeding 80 m s^{-1} above 10 km AGL. The mixed-phase updraft region is between about 4.6 km AGL and 10.5 km AGL. The environment also features extremely large 0–1- and 0–3-km storm-relative helicity (SRH)[5] of >250 and >500 m^2 s^{-2}, respectively, promoting intense mesocyclonic rotation. Conventional wisdom would suggest, then, that this storm is capable of producing very large hail.

Indeed, the time series of hail size metrics (Fig. 14) reveals maximum hail sizes up to nearly 10 cm, substantially larger than produced in the umax41vmax16 case. However, there is otherwise a surprisingly *lower* concentration of severe-sized hailstones, on average by more than a factor of 6, despite more than double the number of initial embryos seeded owing to the finer grid spacing. In other words, though maximum hail sizes approach 10 cm does suggest that, occasionally, the storm is capable of producing giant[6] hail (presumably because of the much greater CAPE), it is not as prolific at consistently producing severe and significantly severe hail as the umax41vmax16 case. These features are qualitatively consistent with Nelson (1983), who found a stronger but narrower updraft and less favorable hail production in a tornadic storm compared to a more prolific hail producer in the two cases he examined.

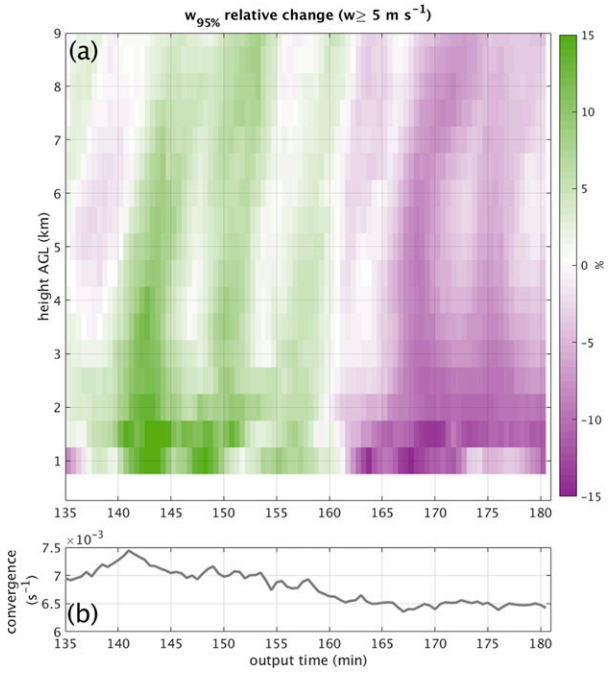

FIG. 11. (a) Time–height display of the relative change in 95th-percentile updraft speed ($w_{95\%}$) within $w \geq 5$ m s^{-1}, shaded in percent according to the scale. Relative changes are computed using the time-averaged $w_{95\%}$ at each altitude. (b) The conditionally sampled mean convergence magnitude (>5 × 10^{-3} s^{-1}) associated with the storm's cold pool.

[5] Computed using the Bunkers et al. (2000) method.

[6] Here, we follow the proposed naming conventions in Kumjian et al. (2020) and references therein, where "giant" refers to hail ≥ 10 cm in maximum dimension, and "gargantuan" refers to hail ≥ 15 cm in maximum dimension.

Brought to you by Pennsylvania State University, Paterno Library | Unauthenticated | Downloaded 10/11/21 01:54 PM UTC

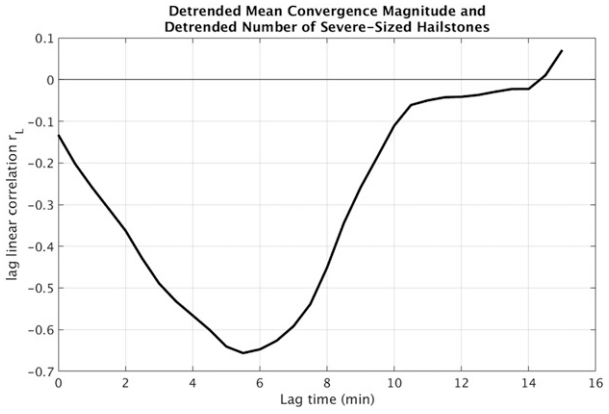

FIG. 12. Lag correlation coefficient between the detrended lowest-model-level mean convergence magnitude (conditionally sampled for magnitudes $> 0.005\,s^{-1}$) and the detrended number of severe-sized hailstones produced.

To understand these differences in hail production, we again examine the relationships between storm attributes and hail production. Figure 15 shows a corner plot, constructed as in Fig. 9. Compared to the umax41vmax16 storm, the updraft $w \geq 15\,m\,s^{-1}$ area is much smaller[7] ($<55\,km^2$ at 5.625 km AGL compared to $>110\,km^2$), though the updraft speeds are greater as measured by both the mean w and $w_{95\%}$. Additionally, both the storm-relative $v > 0$ wind and the mean favorable horizontal wind speeds within the $\geq 15\,m\,s^{-1}$ updraft generally are larger than in the umax41vmax16 case, suggesting faster hailstone advection across the updraft and consequently shorter residence times, and thus less favorable pathways for hail production. Unlike in the umax41vmax16 case, the number of severe-sized hailstones is not as strongly tied to certain portions of the storm attribute parameter space. The times of greater hail production occur for *generally* smaller $v > 0$ and mean favorable horizontal wind speeds, for example, but the distinction is not as clear as in Fig. 9 for the umax41vmax16 case.

To further understand the evolving hail production in the El Reno storm, we compare composited midlevel storm structures during "large-hail" times (109–110 min) and "small-hail" times (100–103 min). Composites taken at 5.625 km AGL and their difference are shown in Fig. 16. During both large- and small-hail times, the storm exhibits a strong updraft, mesocyclone, and well-defined bounded weak echo region (BWER), all hallmarks of an intense supercell. At small-hail times, the updraft has more of a "horseshoe shape" with compact vortices in both the northern and southern ends. Based on a large number of idealized supercell simulations, Peters et al. (2020) found that horseshoe-shaped updrafts apparently are more common in environments featuring large storm-relative helicity at low levels, consistent with the El Reno supercell's

[7] In part, this is a result of differing horizontal grid spacing (e.g., Lebo and Morrison 2015). However, the storm simulation in the next subsection demonstrates there are physical reasons for this, too.

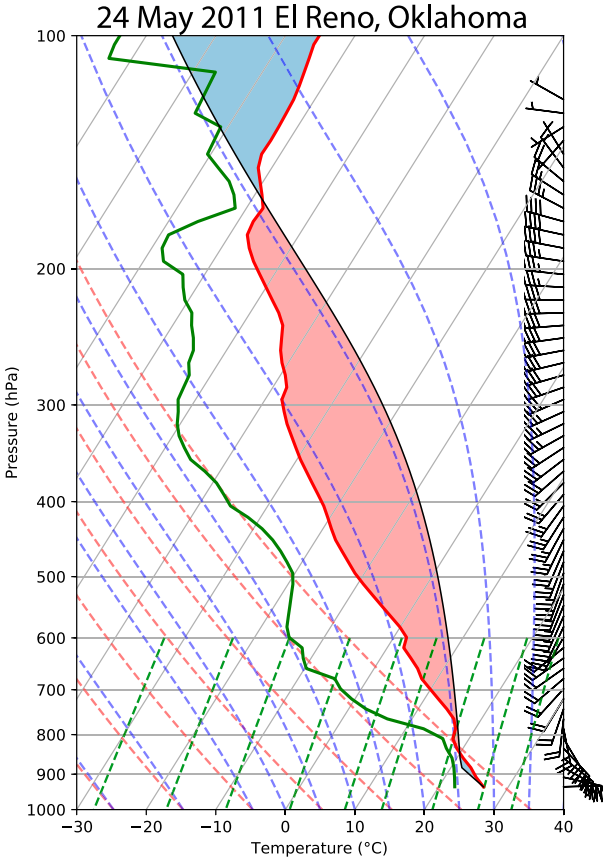

FIG. 13. Input sounding for the 24 May 2011 El Reno simulation. The wind barbs are in $m\,s^{-1}$, with a half barb and whole barb representing 2.5 and $5.0\,m\,s^{-1}$, respectively. The salmon-colored shading represents the region of positive buoyancy for a surface-based parcel. The parcel path is indicated by the thin solid black line; here the surface-based CAPE = $4211\,J\,kg^{-1}$. The blue shading indicates the region of negative buoyancy for the surface-based parcel; here the surface-based CIN = $-17.6\,J\,kg^{-1}$. The LCL height is 879.8 hPa, and the LFC height is 844.5 hPa.

environment. Further, Dahl (2017) suggested that compact vortices in midlevel updrafts like those seen in Fig. 16 may be related to the ingestion of baroclinic vorticity-augmented air from low levels; the large ($>4000\,J\,kg^{-1}$) CAPE in the environment of the El Reno storm certainly promotes stronger cold pools and thus, potentially, increased low-level baroclinic vorticity production. During small-hail times, an anticyclonic vortex is evident on the southern flank of the updraft. A few minutes later, at the large-hail times, the updraft appears more circular.

The difference field shows an anticyclonic vortex on the southeast flank of the updraft, to the east of the anticyclonic vortex observed during the small-hail times composite. This indicates that the flow curvature is less cyclonic and/or more anticyclonic in the eastern side of the updraft in the large-hail times. Specifically, the storm-relative flow in the eastern half of the mesocyclone and updraft has increased eastward ($u > 0$) and northward ($v > 0$) components. Unlike the previous case, there is a more significant region of $v < 0$ flow in the western half of the

Brought to you by Pennsylvania State University, Paterno Library | Unauthenticated | Downloaded 10/11/21 01:54 PM UTC

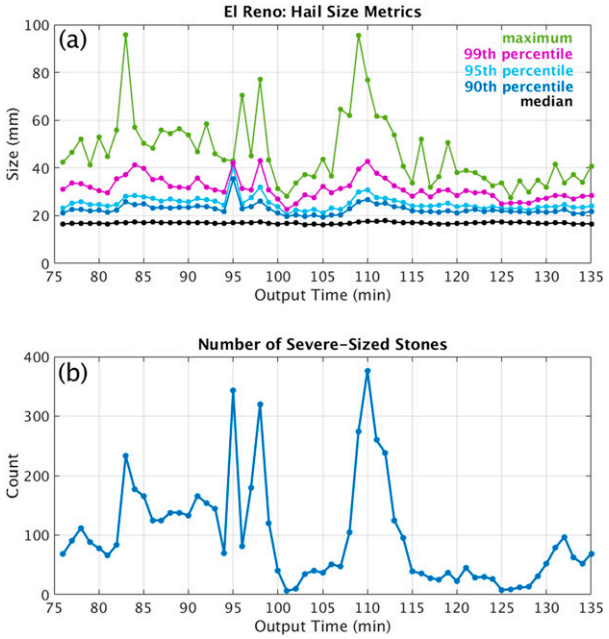

FIG. 14. As in Fig. 2, but for the El Reno storm.

updraft; this north-to-south flow strengthens at large-hail times, collocated with an increase in the updraft intensity there, possibly indicating a new pathway for hail growth.

Indeed, these structural changes lead to differences in hail production through changes in embryo source regions and hailstone growth trajectories. Figure 17 shows embryo source regions, colored by final size attained, at 5.625 km AGL. At $t = 109$ min (a large-hail time), a broader region of initial embryo sources resulting in significant growth is evident, particularly on the northern and northeastern flanks of the updraft. Further, larger maximum final sizes are attained by embryos on both the northern and southern flanks. Embryos seeded in the northern flank would be swept around the north side of the mesocyclone. Given the stronger north-to-south flow at $t = 109$ min, it is possible that more of these initial embryos could be swept around to a favorable ingestion region on the updraft's southern flank, thus opening new pathways for hail production. Figure 18 compares the trajectories for 5-mm embryos seeded in this region. Indeed, at $t = 109$ min, we see a new pathway opened for hail growth: embryos seeded northeast of the updraft are swept around the north side of the mesocyclone, descend around its west side, and are swept quickly from north to south by the enhanced northerly flow. This allows some embryos to complete a circuit around the south side of the updraft (annotated by greenish lines in Fig. 18), after which they are ingested into the main updraft and grow via the archetypal hailstone pathway (e.g., Browning and Foote 1976). Further, other embryos end up as hailstones in the hook echo appendage feature of the supercell at this time, including some that grow >7.5 cm in diameter.[8] Neither of these pathways is evident in the $t = 101$-min trajectories launched from the same storm-relative region, indicating that indeed these growth trajectories are different. Some hailstones even took two passes through the updraft owing to the full-circuit trajectory, allowing for greater growth. These new pathways at $t = 109$ min are present for all four embryo sizes considered, but, for clarity, only the trajectories from 5-mm embryos are shown in Fig. 18. As shown in Fig. 17, embryos taking these full-circuit trajectories attain greater final sizes than those initialized at the same storm-relative location at the earlier time, which do not take the full-circuit trajectories.

The stronger mesocyclonic flow that opens the full-circuit trajectory and allows the growth of very large hail that falls into the hook echo may be detectable by Doppler radar. As a crude estimate of how a Doppler radar may observe these storm structural differences, we simulated the radial component of the wind when viewed from a ground-based radar scanning at 5° elevation. This calculation was performed for every 0.5° in azimuth. Figure 19a shows an example of the simulated radial velocity (v_r) at the small-hail time ($t = 101$ min), which features a prominent cyclonic shear signature associated with the mesocyclone. The v_r values are used to obtain the rotational velocity (defined as maximum outbound minus minimum inbound v_r values) at each assumed azimuth angle; these calculations are performed at each height level, leading to a distribution of rotational velocity values at each height. The difference in large- and small-hail time median and mean values of the rotational velocities as a function of height are shown in Fig. 19b. In the lowest ~2.5 km of the mixed-phase region, the large-hail time features greater median and mean rotational velocities. This suggests that, on average, a Doppler radar would likely detect greater mesocyclone intensity in the lower portion of the mixed-phase region during times of greater hail production. Although the differences in rotational velocity are small and may be challenging to observe in real time, these calculations are consistent with observations by Blair et al. (2011), Witt et al. (2018), and Gutierrez and Kumjian (2021), who showed larger hail-size classes were associated with stronger radar-observed rotational velocities. The stronger average rotational velocity and thus inferred stronger mesocyclone in the hail growth region could reflect the opened pathways leading to enhanced hail growth.

Interestingly, some of the output times toward the end of the simulation, which coincide with times of lesser hail production, featured a tornado-like vortex at low levels. Time–height depictions of storm-relative $v > 0$ flow within the updraft (not shown) reveal strong southerly winds being advected upward into the hail growth region during these times. Strong southerly winds in the hail growth region, as shown above and in our previous work (KL2020) tend to be unfavorable for hail production. We speculate this may be one contributing factor to anecdotal and limited polarimetric radar-based evidence (Kumjian and Ryzhkov 2008) that tornadic supercells seem to be less-prolific large-hail producers than nontornadic supercells.

To summarize the findings from the El Reno case, hail sizes are increased (albeit in small numbers) owing to the full-circuit trajectory that opens up during times of strong mesocyclonic rotation, leading to embryos that participate in significant growth and achieve larger sizes. Other trajectories at times of a stronger

[8] Giant and gargantuan hail has been observed in the hook-echo region of some storms (e.g., Witt et al. 2018).

Brought to you by Pennsylvania State University, Paterno Library | Unauthenticated | Downloaded 10/11/21 01:54 PM UTC

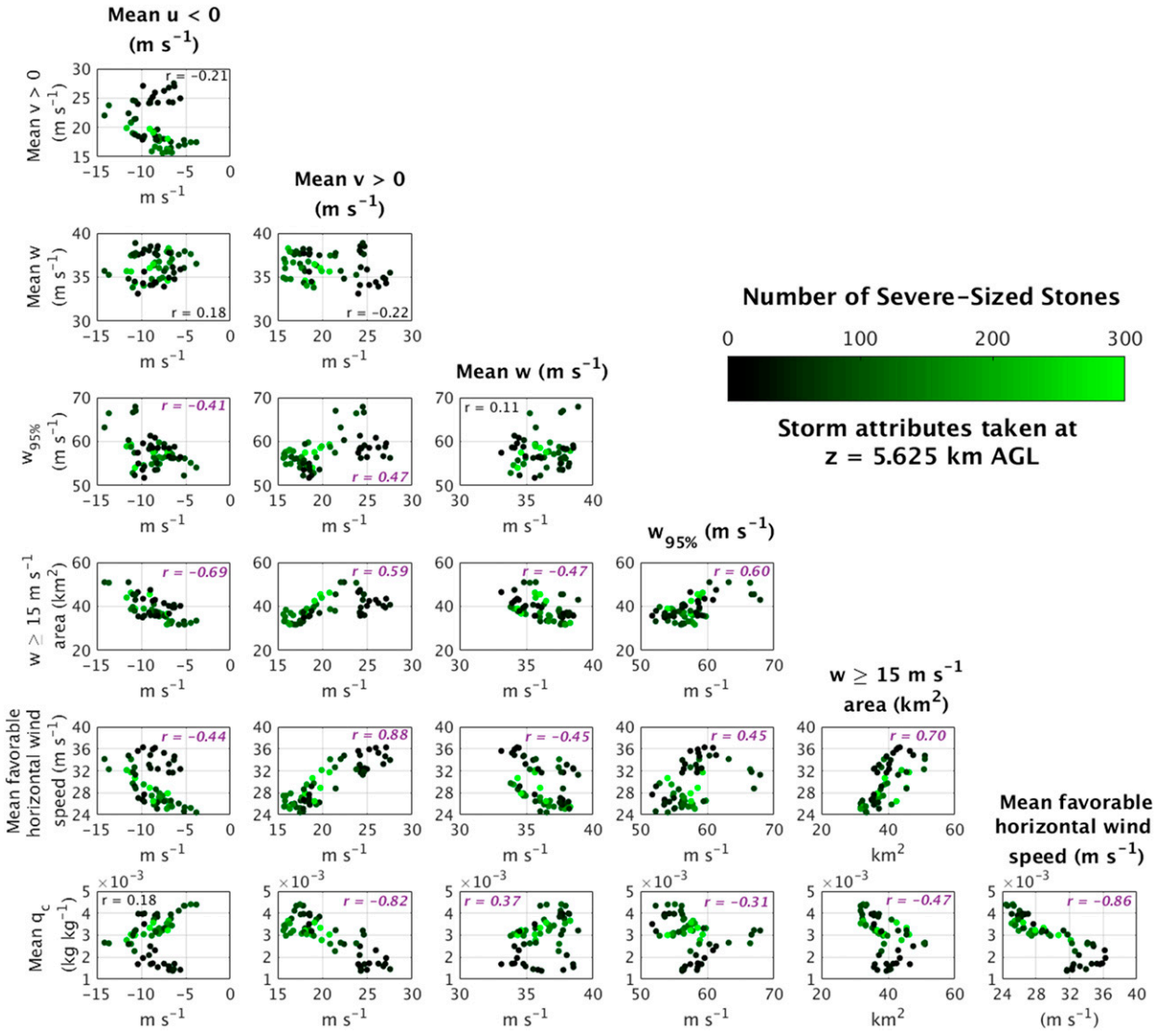

FIG. 15. Corner plot, as in Fig. 9, but for the El Reno storm.

mesocyclone lead to extremely large hail falling out in the low-level hook echo. However, there is a delicate balance that likely limits the quantity of large-hail production: though stronger airflow opens up new pathways for hail growth, in general it leads to reduced residence times and thus curtails the growth potential for most trajectories. In other words, *compact, strongly rotating updrafts appear to be detrimental for the production of large quantities of hail, including severe-sized hail, but they could lead to a small number of embryos following favorable pathways*. Further, the presence of a tornado-like vortex appears to be detrimental to large-hail production owing to the vertical advection of strong southerly flow into the hail growth region.

c. *The umax41-El Reno supercell*

The umax41vmax16 and El Reno storms form in very different environments and reveal different mechanisms for the evolution of hail production. To isolate the processes leading to these different mechanisms, we run a third simulation (umax41-El Reno) that uses the El Reno thermodynamic profile, but with the umax41vmax7 idealized quarter-circle hodograph (i.e., a vertical wind profile characterized by predominantly straight-line shear; Fig. 1, purple line). The idea is to 1) maintain a very strong updraft, in part produced by the large CAPE in the El Reno environment, 2) maximize the updraft breadth by using the umax41vmax7 hodograph for larger deep-layer shear and associated greater low-level inflow (see DK17; Warren et al. 2017; Trapp et al. 2017; Peters et al. 2019; KL2020), and 3) minimize the southerly flow component (hence the vmax7 portion of the hodograph; see DK17 and KL2020) in an effort to maximize hail production. To put it bluntly, we attempt to ''Frankenstein'' an environment into being conducive for large-hail production based on the two prior experiments above and our previous findings.

Brought to you by Pennsylvania State University, Paterno Library | Unauthenticated | Downloaded 10/11/21 01:54 PM UTC

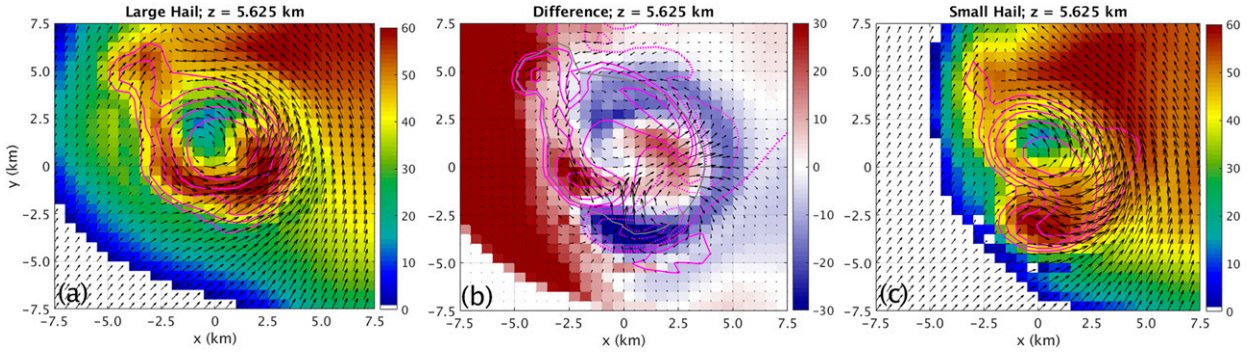

FIG. 16. Composite of (a) large-hail times (109–110 min) and (c) small-hail times (100–103 min) and (b) their difference, at 5.625 km AGL. In each, simulated reflectivity factor is shown (shaded according to scale in dBZ), overlaid with contours of w (10, 20, 30, and 40 m s^{-1}, magenta lines) and horizontal storm-relative wind vectors (black arrows). (b) The difference in the composites (large minus small); w differences are in magenta contours (5, 10, 20, 30, and 40 m s^{-1}), with dashed for negative and solid for positive. The horizontal wind vectors (u, v, black) show the vector difference. The gray solid line in (b) represents the 10 m s^{-1} updraft contour from the large-hail-times composite, for reference.

The simulation again produces a strong supercell storm, with maximum updraft speeds approaching 80 m s^{-1}. Compared to the El Reno simulation, both the mean w and $w_{95\%}$ within $w \geq 15$ m s^{-1} are substantially weaker below about 7 km AGL, which is within and below the hail growth region (~4.4–10.6 km AGL correspond to 0° and −40°C in-updraft temperatures, respectively). This weaker updraft exists despite both storms encountering the same thermodynamic environment. The difference in low-level updraft intensity therefore arises owing to difference in hodographs between the simulations (cf. Fig. 1).

The El Reno hodograph features very large low-level wind shear (>25 m s^{-1} 0–3-km bulk wind difference) and 0–3-km SRH (>500 m^2 s^{-2}). Increased low-level vertical wind shear lowers the base of the midlevel mesocyclone by enhancing the tilting of environmental horizontal vorticity into the vertical and thereby leads to a lower altitude at which significant vertical vorticity arises (Markowski and Richardson 2014). This vertical vorticity is associated with an upward-directed nonlinear dynamic perturbation pressure-gradient acceleration at lower levels. If the low-level environmental horizontal vorticity has a significant streamwise component (reflected in greater magnitudes of SRH), the vertical vorticity and updraft regions will be more spatially correlated (e.g., Davies-Jones 1984; Markowski and Richardson 2010; Coffer and Parker 2017; Peters et al. 2020). The upward perturbation pressure-gradient acceleration is then better aligned with the updraft, strengthening it further. Together, then, these effects lead to stronger low-level updrafts in cases with large SRH. In contrast, the straighter hodograph in the umax41-El Reno experiment

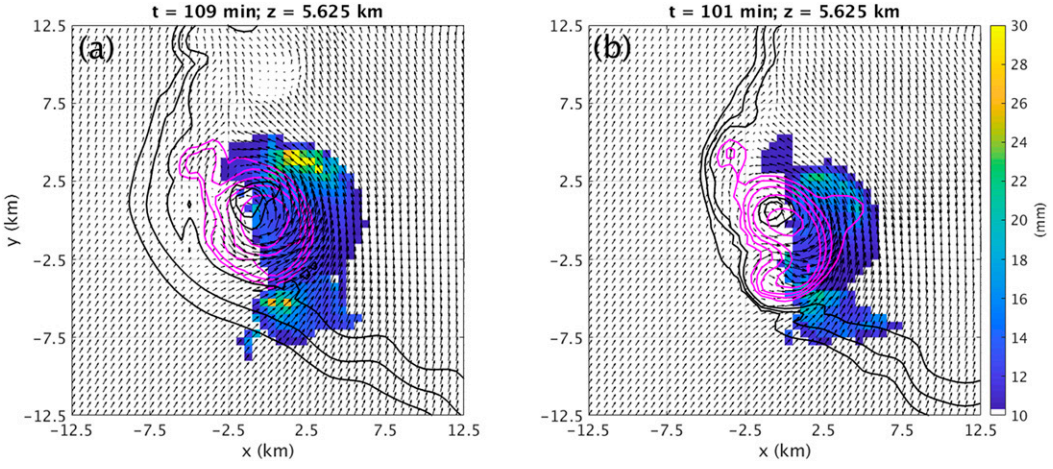

FIG. 17. Horizontal cross section showing embryo source regions at 5.625 km AGL, colored by final size attained (shading, in mm) for (a) a time of maximum hail production (t = 109 min) and (b) minimum hail production (t = 101 min). Black contours are simulated radar reflectivity factor values of 10, 20, and 30 dBZ. The magenta lines show the updraft 10, 20, 30, 40, and 50 m s^{-1} contours. Horizontal storm-relative winds at this height level are given by black arrows.

Brought to you by Pennsylvania State University, Paterno Library | Unauthenticated | Downloaded 10/11/21 01:54 PM UTC

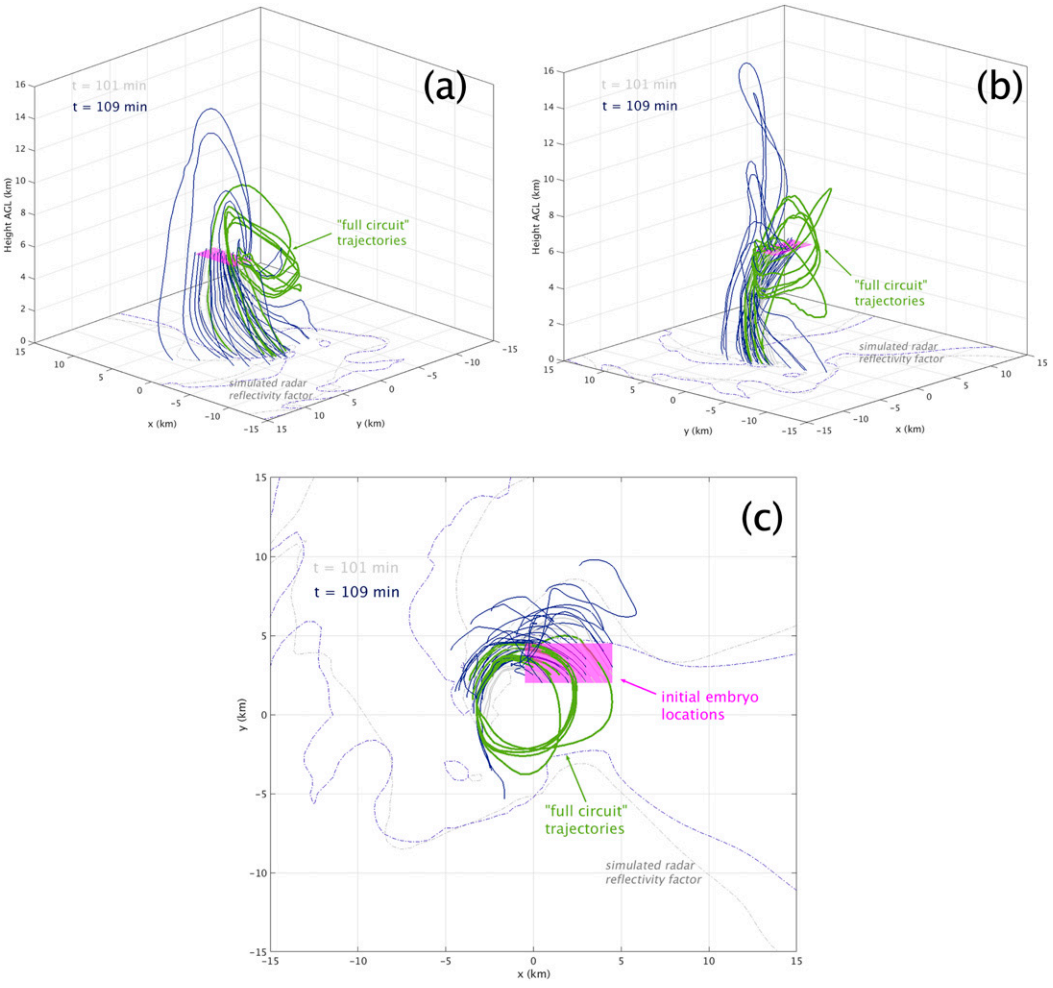

FIG. 18. Different views of 3D trajectories seeded in the region northeast of the primary updraft (which is shaded in magenta). Gray lines are from a small-hail time $t = 101$ min, whereas blue lines are from a large-hail time $t = 109$ min. Calculations are shown for 5-mm embryo size. Low-level simulated radar reflectivity factor contours of 10 and 50 dBZ are provided for reference, colored according to the time. Views are from (a) the south, (b) the west, and (c) above. The full-circuit trajectories are highlighted in green in each panel, and are associated with the stronger mesocyclone at large-hail times ($t = 109$). These are absent at $t = 101$ min.

produces a weaker updraft below 7 km AGL that is also broader than that of the El Reno storm, as expected, and by design. Previous work suggests both these factors—a broader and more moderate updraft—should lead to enhanced hail production (e.g., Nelson 1983; DK17; KL2020).

The hail-size metrics for this simulation are shown in Fig. 20. Compared to the El Reno storm, the umax41-El Reno storm produces a similar maximum size (~10 cm), but otherwise consistently *larger* 99th-, 95th-, 90th-, and 50th-percentile sizes (cf. Fig. 14). In particular, the umax41-El Reno storm produces approximately *an order of magnitude greater* number of severe-sized stones than the El Reno storm. This demonstrates that, given the same thermodynamic environment, the environmental wind profile can play a strong role in modulating hail production (e.g., DK17).

The umax41-El Reno time series of hail metrics—particularly the number of severe-sized hailstones—displays a pronounced periodicity not evident in the El Reno case. Upon visual inspection of the storm structures at midlevels, we found that the umax41-El Reno storm nearly continuously sheds anticyclonic vortices from the north or northeast updraft flanks. Such vortex shedding occurred approximately during output times 82–84, 94–100, 108–109, 117–123, and 124–130 min. Qualitatively, these times appear related to the peaks in hail production, particularly the number of severe-sized stones (Fig. 20b); these times are highlighted in the figure. A Fourier analysis applied to the number of severe-sized hailstones time series reveals a relative maximum at 400-s time scales, or 6.67 min. Though less pronounced, the umax41vmax16 also displays a seemingly periodic behavior in the number of severe-sized stones (see Fig. 3b); the Fourier analysis applied to that storm shows a peak at 552 s (or 9.2 min). We are unaware of observations documenting the time scales for such anticyclonic vortex shedding. However, these time scales do compare favorably to high-resolution radar

Brought to you by Pennsylvania State University, Paterno Library | Unauthenticated | Downloaded 10/11/21 01:54 PM UTC

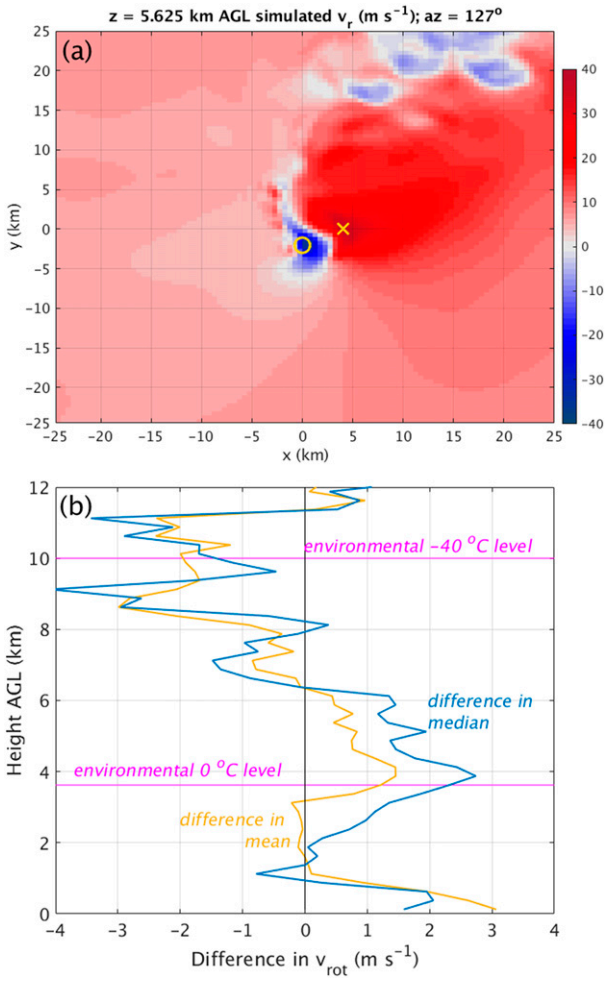

FIG. 19. (a) Example simulated radial velocity (v_r) field (in m s^{-1}, shaded according to scale) from the small-hail time (t = 101 min) of the El Reno storm, taken at 5.625 km AGL. The golden circle and × markers indicate the location of the maximum inbound and outbound velocities, respectively. In this example, the azimuth of the "radar" is 127°, which provides the maximum rotational velocity (v_{rot}, defined as the maximum outbound minus minimum inbound velocity) for this time and height. (b) Vertical profiles of the difference in the mean (goldenrod) and median (blue) v_{rot} between large-hail and small-hail times; positive differences indicate stronger v_{rot} during the large-hail times. The environmental 0° and −40°C levels are annotated by magenta lines.

observations of mesocyclone cycling in supercells. For example, Beck et al. (2006) found ~6 min between successive mesocyclones in a case study with high-resolution mobile radar data, and French et al. (2008) observed a mean and median time between new circulations developing of 11.6 and 8 min, respectively. If the processes of forming and shedding an anticyclonic circulation in supercells are similar to those of cyclonic circulations, similar time scales could be expected. As discussed earlier, this anticyclonic vortex shedding is associated with an updraft expansion and weakening, leading to more favorable conditions for hail production.

Storm attributes as a function of hail production are shown in the corner plot (Fig. 21). Similar to the umax41vmax16 case, we see a tendency for a weaker updraft (both in terms of mean w and $w_{95\%}$), weaker mean favorable horizontal flow, and weaker $u < 0$ and $v > 0$ components within the updraft during times of enhanced hail production. The relationship between hail production and storm attributes is more consistent between the umax41-El Reno storm and the umax41vmax16 storm rather than the El Reno storm, implying that the hodograph can play a strong role in the interplay between storm behavior and hail production.

To examine the storm structures responsible for the evolving hail production behavior in the umax41-El Reno storm, we again take composited horizontal slices through the hail growth region at large-hail times (80–84 min), small-hail times (103–106 min), and their difference, displayed in Fig. 22. The storm exhibits a broad, strong updraft with an "open vortex" mesocyclone structure (Dahl 2017) dissimilar from the El Reno storm's compact, closed mesocyclone. The difference fields display two cyclonic vortices on the north flank of the updraft, implying more cyclonic and/or less anticyclonic flow during large-hail times. Indeed, the small-hail-times composite features two anticyclonic vortices to the north and northeast flanks of updraft, reflecting the anticyclonic vortex shedding discussed above. The difference fields also reveal an expansion of the updraft region northward and eastward, a weakening of the updraft core speed, and a slowing of the $v > 0$ horizontal wind component in the eastern portion of the updraft at large-hail times, similar to the umax41vmax16 case. Unlike the umax41vmax16 case, however, no strong lagged correlations were found between low-level convergence magnitude and updraft strength (not shown).

In summary, the umax41-El Reno storm features a periodicity to its hail production similar to the umax41vmax16 case. The straighter hodographs in these two cases promote weaker mesocyclones and anticyclonic circulations forming periodically on the updraft flanks (e.g., Markowski and Richardson 2010). This is in contrast to the more persistent and stronger mesocyclone that is better collocated with the updraft in the El Reno case, resulting from its loopier hodograph. Unlike the El Reno case, the umax41-El Reno and umax41vmax16 cases did not feature full-circuit trajectories owing to the differences in mesocyclone structure. These results indicate that the hodograph shape (i.e., straighter versus loopier) plays a large role in governing updraft properties, behavior, and thus hail production. Increased hail sizes and concentrations of severe hail occurred at times of updraft expansion and weakening, also associated with weaker horizontal flow in the updraft, following the shedding of anticyclonic vortices. Compared to the umax41vmax16 case, however, the maximum hail sizes produced in the umax41-El Reno storm are much larger, owing to the slower $v > 0$ wind component in the updraft with comparable 95% updraft speeds.

4. Four-dimensional trajectories

The previous section analyzed hail production at different stages throughout the storms' evolution, but assumed

Brought to you by Pennsylvania State University, Paterno Library | Unauthenticated | Downloaded 10/11/21 01:54 PM UTC

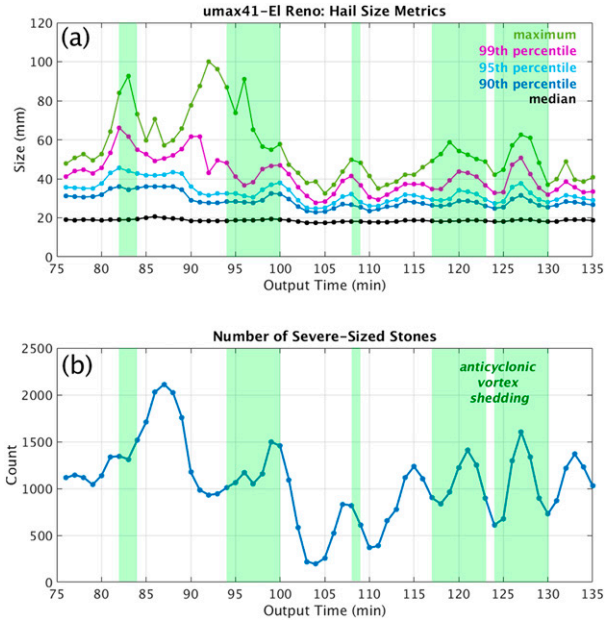

FIG. 20. Time series of umax41-El Reno hail size metrics, as in Figs. 2 and 14. Here, the green bars represent the approximate times of anticyclonic vortex shedding.

steady-state fields for the duration of the trajectory calculations at a given model output time. This prompts the question, How do time-varying storm fields affect hail production? To answer this question, we use the umax41vmax16 storm simulation (the first case analyzed above), owing to the availability of 30-s output files. Beginning at 135 min into the simulation, we seed embryos as described in section 2. The embryos are advected throughout the storm, as before, but now the background supercell simulation fields are updated every 30 s. Thus, as the hailstones are growing along their trajectories, the fields are changing, emulating an evolving storm. We repeat the embryo insertion every 2 min. One limitation of this approach is that, as the embryo insertion time gets later, the number of output times available for computation decreases. Thus, we stop inserting embryos into the storm simulations at output times after 163 min; after this time, a large number of the embryos are still within the simulated storm (i.e., have not yet finished growing) by the time the last output file is reached, which would bias the results when comparing to earlier times.

Figure 23 shows the distribution of final hail sizes attained by the embryos inserted at each of these start times. Compared to Fig. 3, we see a similar spread in the distributions, with maximum sizes for each start time ranging between about 4.5 and 6.0 cm. This suggests that, in general, the 4D trajectories lead to similar final numbers and sizes of hail to the "steady-state" calculations applied at each output time, and that the variability in hail production owing to storm evolution is similar for both approaches.

Figure 24 is the time series of hail size metrics for the evolving 4D trajectories, with the steady-state fields calculations shown for comparison. The comparison reveals similar ranges in values for each metric between the 4D trajectories and steady-state fields. The time trends for the larger size metrics for the evolving fields appear to lead those of the steady-state fields; for example, the maximum size increases around ~153 min for the evolving fields, but not until ~166 min for the steady-state fields. This can be explained by how we implemented the different approaches. For the evolving fields, the final hail size statistics are plotted at the *time the embryos were initialized*, regardless of how long it takes the hailstones to grow to their final sizes. Embryos seeded at a given time—particularly those initially farther from the updraft—may not reach the hail growth region until several minutes later, when the storm's structure and hail production capabilities may have changed. In contrast, for the steady-state fields approach, the hail size statistics are a result of storm structures *at those times*. Thus, 4D trajectories will show trends in the hail size metrics earlier than those in the steady-state fields tests. We see a similar pattern in the time series of number of severe-sized hailstones (Fig. 25), where the counts are similar in value, but the evolving fields trend leads that of the steady-state fields, for the same reasons. The 4D trajectories hail size metrics also appear smoother than those of the steady-state fields. This occurs for two reasons. First, embryo insertion was performed every 2 min, so the metrics are computed at coarser temporal resolution. Second, transient storm structures that may favor or disfavor hail production are "locked" in place in the steady-state simulations; in contrast, in the 4D trajectories, growing hailstones may not experience these structures for long enough to significantly impact the final sizes.

Figure 26 shows 5.75-km AGL embryo source maps for the steady-state fields and the evolving fields. These maps show the final size attained by an embryo starting at a given location, for all embryo sizes. The general source regions do not change considerably in location. These source regions are controlled by the base-state environment and storm-relative winds around the storm, and in general are relatively steady throughout the time period shown (and others, not shown for brevity). Rather, the final sizes attained by embryos originating in these locations are affected by the details of the trajectories, including the airflow components and supercooled liquid water content. These details change as the storm evolves, but these results show both the steady-state fields and 4D trajectories approaches lead to similar embryo source regions, similar resulting hail sizes, and similar evolving behavior.

There are benefits and limitations to each of these approaches. Advantages of the steady-state approach include 1) the storm fields are "frozen," allowing for direct assessment of what structural features are favorable for hail production, and 2) the calculations are computationally less expensive. An obvious limitation is that real storms are not frozen in time. However, we suggest that, given their quasi-steady appearance on radar, supercell storms are nearly continuously producing potential hail embryos, and embryos at the "right place and the right time" may benefit from favorable storm structures at those times. Advantages of the evolving fields approach include 1) it represents a more natural evolution of hail production in that embryos may not fully benefit from favorable storm structures if they are not persistent, and 2) it can be used

Brought to you by Pennsylvania State University, Paterno Library | Unauthenticated | Downloaded 10/11/21 01:54 PM UTC

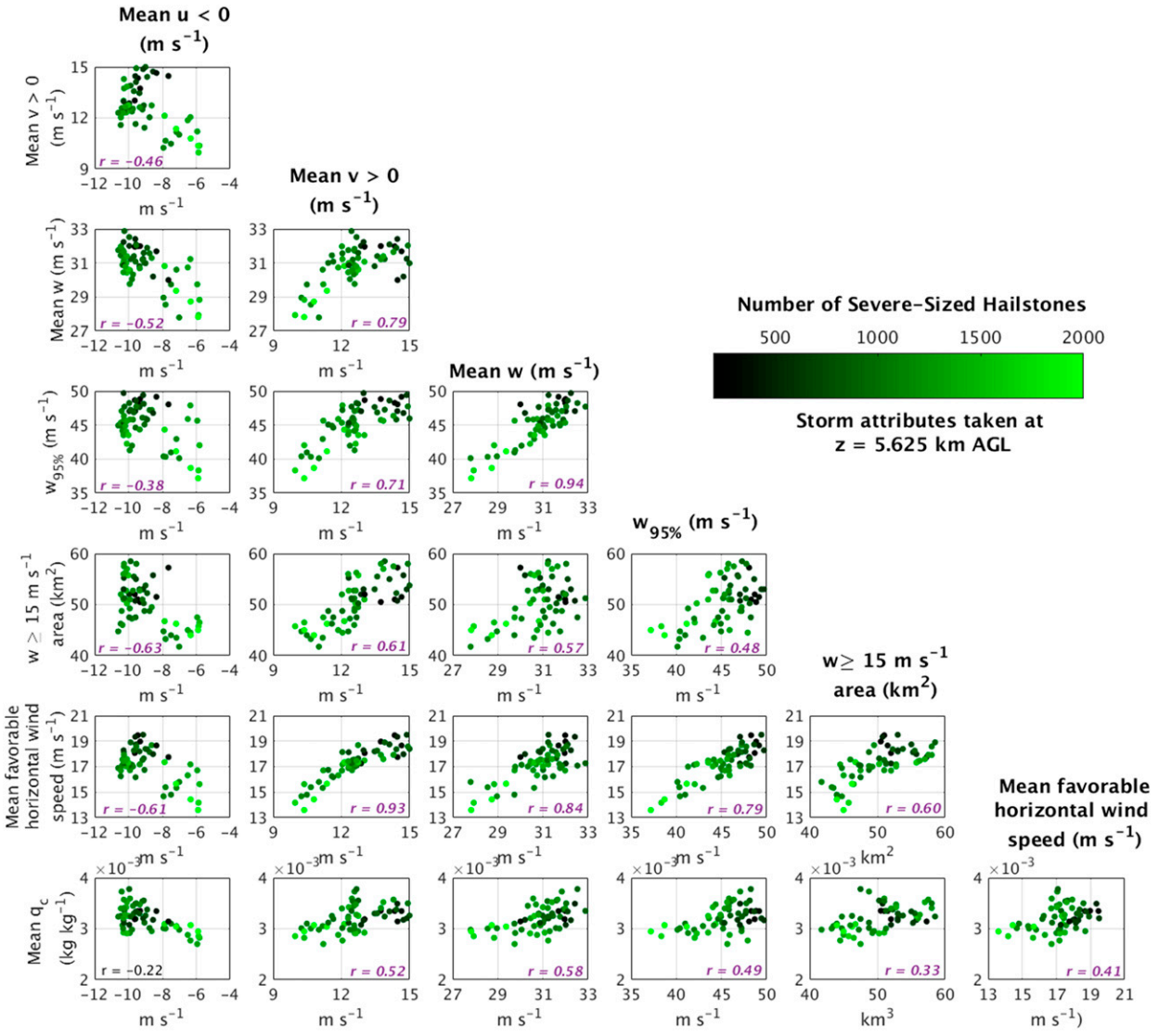

FIG. 21. Corner plot, as in Figs. 9 and 15, but for the umax41-El Reno storm.

to more realistically determine the relative times and locations at which hail may reach the surface. The main disadvantage of this approach is the computational expense. The consistency between the two approaches in terms of bulk hail statistics is encouraging, and suggests that both may be useful for various research or operational purposes.

5. Summary and discussion

We used idealized CM1 simulations of three supercell storms coupled with the hail growth and trajectory model from KL2020 to explore whether or not hail production varies throughout storm evolution, assuming an unchanging, homogeneous base-state environment. We measured changes in hail production by assessing different percentiles of the distribution of final hail sizes produced by the trajectory calculations, as well as the number of trajectories resulting in severe-sized hailstones. The main takeaways from this study are as follows:

- Hail production does exhibit variability throughout the supercell storm life cycle. These changes in hail production can be substantial, with maximum sizes varying by as much as a factor of 2, and the number of severe-sized stones varying by more than a factor of 5 over 45–60-min periods during the mature phase of the simulated supercell storms.
- Variability in hail production in the simulated supercells arises owing to changes in updraft properties, which themselves arise from (i) changes in low-level convergence, which are manifested as upward-propagating perturbations to the updraft speed that move into the hail growth zone, and (ii) internal storm dynamics including anticyclonic vortex shedding and/or storm splitting, and the response of the airflow

Brought to you by Pennsylvania State University, Paterno Library | Unauthenticated | Downloaded 10/11/21 01:54 PM UTC

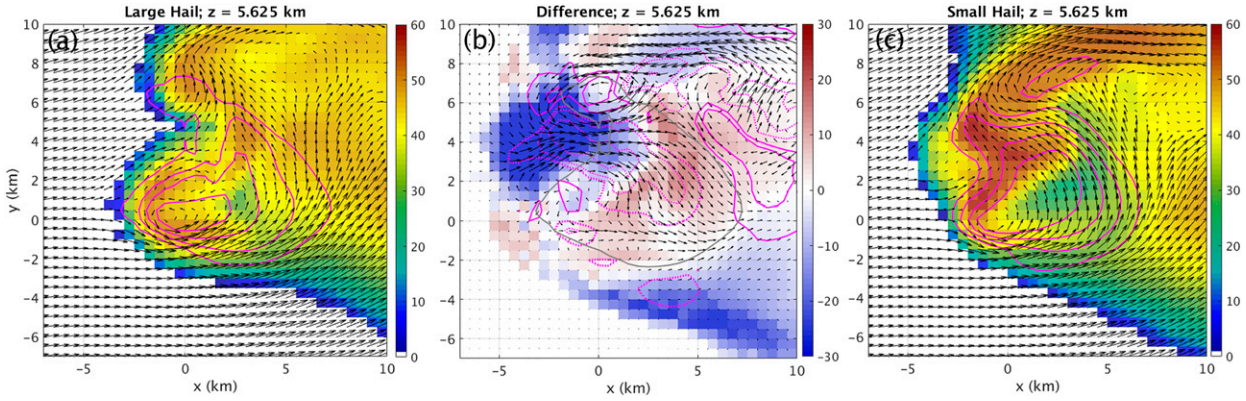

FIG. 22. Comparison of storm structures during large-hail times (80–84 min) and small-hail times (103–106 min), taken at $z = 5.625$ km AGL. In each, simulated reflectivity factor is shown (shaded according to scale, in dBZ), overlaid with contours of w (10, 20, 30, and 40 m s^{-1}, magenta lines) and horizontal storm-relative wind vectors (black arrows). (b) The difference in the composites (large minus small); w differences are in magenta contours (5, 10, 20, 30, and 40 m s^{-1}), with dashed for negative and solid for positive. The horizontal wind vectors (u, v, black) show the vector difference. The gray solid line in (b) represents the 10 m s^{-1} updraft contour from the large-hail-times composite, for reference.

fields and supercooled liquid water content fields to these events.

- The evolution of hail production is affected by hodograph shape. Straighter hodographs (i.e., those with primarily unidirectional shear) tended to lead to more prolific hail production, owing to those environments producing wider updrafts with broader moderate updraft regions, and weaker mesocyclonic flow. In contrast, the highly curved hodograph from the 2011 El Reno tornadic supercell event led to a storm with a stronger but more compact updraft, which occasionally produced ~10-cm hail but was less prolific in severe hail production overall than the straighter hodograph cases.
- Peaks in hail production were periodic for the straighter hodograph cases and tended to be associated with anticyclonic vortex shedding and/or storm splitting. In particular, the resultant changes in storm structure led to relatively weaker updrafts and a reduced storm-relative southerly[9] flow speed in the updraft, and consequently longer residence times and thus larger hail.
- The strongly curved hodograph case produced a supercell with a strong mesocyclone. ''Full circuit'' trajectories opened up at times of stronger mesocyclonic flow, and could indicate a new pathway for larger hail growth. The hailstones produced by these full-circuit trajectories are larger than those arising from embryos seeded in similar storm-relative locations at times when the full-circuit pathway is not open. Additionally, very large hail (>7.5 cm in diameter) falls into the hook echo at the time when full-circuit trajectories are activated, although these stones do not arise from the full-circuit trajectories themselves. This is consistent with observations: giant and gargantuan hail has been observed in this region of the hook echo (e.g., Witt et al. 2018), and radar-observed strong mesocyclonic rotation seems to be an indicator of the potential for such large hail (e.g., Blair et al. 2011; Witt et al. 2018; Gutierrez and Kumjian 2021).
- For the first time, detailed hailstone growth trajectories were driven by evolving fields using a supercell simulation with 30-s output. Compared to running the trajectories on each output file independently assuming steady-state fields, the

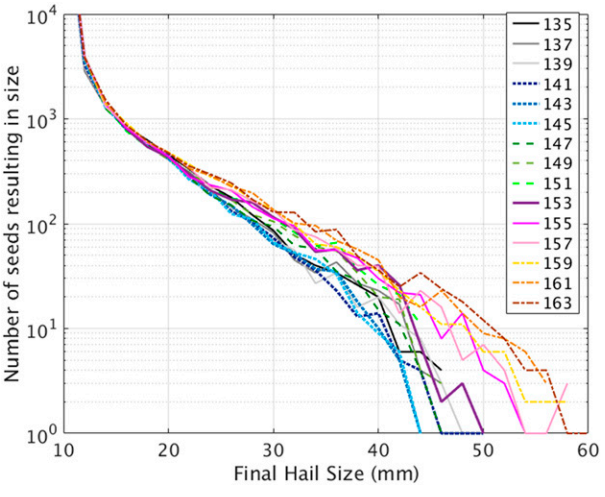

FIG. 23. Calculations for the umax41vmax16 simulation with the ''4D trajectories'' approach, showing the resulting distributions of final hail sizes for different start times, according to the legend. Values in the legend indicate output times (min) at which embryos were initialized. All four embryo sizes are considered.

[9] Conceptually, this flow component in our simulations represents the right half of the mesocyclone in the Northern Hemisphere, which guides a favorable pathway for growing hailstones across the updraft. The importance of this southerly flow component has been identified in our previous work (KL2020). More generally, this is the flow component orthogonal to the deep-layer shear vector.

Brought to you by Pennsylvania State University, Paterno Library | Unauthenticated | Downloaded 10/11/21 01:54 PM UTC

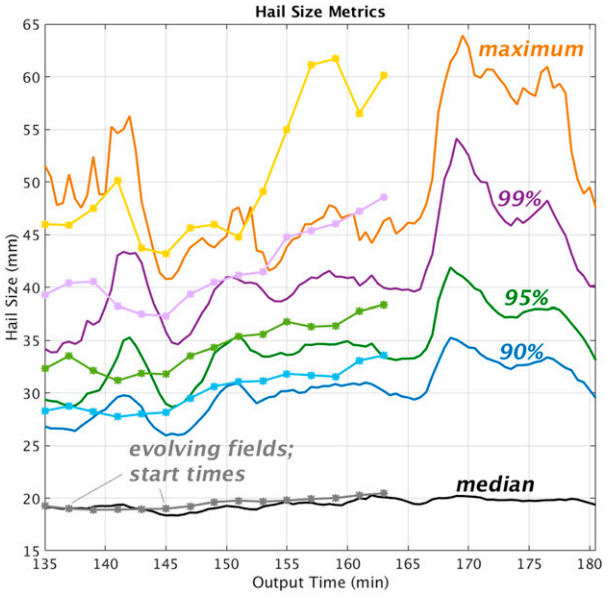

FIG. 24. Comparison of the time series of hail metrics for the umax41vmax16 storm. Steady-state fields are shown as solid lines, evolving fields with lighter colored lines and star markers. The evolving fields marker indicates the time at which embryos were inserted into the evolving simulation.

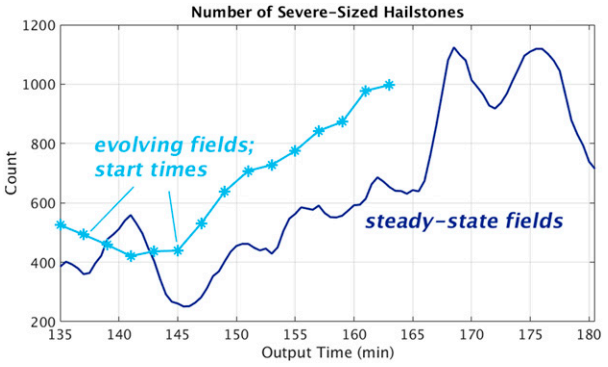

FIG. 25. Time series of number of severe-sized stones for the umax41vmax16 storm. Steady-state fields are shown as solid lines, evolving fields with lighter colored lines and star markers. The evolving fields marker indicates the time at which embryos were inserted into the evolving simulation.

evolving-fields results demonstrated consistent embryo source regions, consistent distributions of final hail sizes, and similar temporal variability of hail production (when accounting for the time needed for some embryos to advect and be swept into the hail growth region).

The difference in behavior between the strongly curved hodograph case (El Reno significantly tornadic supercell) and the straighter quarter-circle hodograph cases is reminiscent of the contrasting cases presented by Nelson (1983). In that study, the nontornadic storm with a weaker mesocyclone was a more prolific hail producer than the tornadic storm. Nelson highlighted storm structural differences including a broader, moderate updraft in the prolific hailstorm versus a stronger, compact updraft in the tornadic storm, with which our results are consistent. An observational analysis of cases with these different hodograph regimes identified (straight vs highly curved) is warranted, with special attention paid to hail size reports and/or radar-based hail indicators around the time of storm splitting or anticyclonic vortex shedding as inferred from, for example, Doppler radar observations.

Previous hail growth studies have used single times with assumed steady state fields (e.g., Heymsfield 1983; Nelson 1983; Ziegler et al. 1983; Rasmussen and Heymsfield 1987; Miller et al. 1988; among many others) or used composites or averages over numerous times (e.g., Grant and van den Heever 2014; DK17; KL2020). This prohibits understanding how subtle storm structural changes could affect hail sizes. Reports from well-documented events (e.g., National Weather Service 2016) do generally depict maximum reported hail sizes varying both along and across the hail swath. Our study is a step toward understanding why such variability exists, and suggests that this variability should be considered in future studies. In terms of the approach for simulations (steady-state fields at each time step versus evolving fields), steady-state calculations maybe better to isolate storm attributes *at that time* that are conducive to hail. Assuming that in supercell storms, embryos and other ingredients are generally present, just in different amounts, the steady-state approach shows us the storm structural features one should look for in, for example, radar observations, to indicate a heightened or lessened hail threat. Examples of such storm structural features include updraft width, variations in mesocyclone strength, and the presence and behavior of anticyclonic rotation on the updraft flank.

Our results have showed considerable changes to the concentrations and maximum sizes of damaging hail throughout a storm's evolution, even in a homogeneous base-state environment. Unless a storm is adequately sampled throughout its evolutionary cycle, snapshots of hail sizes from ground reports very likely will insufficiently resolve the true nature of hail production. For illustrative purposes, we simulated a "hail swath" by translating the hail sizes and fallout locations from each umax41-El Reno simulation output file with an average storm motion of $u_{\text{storm}} = 15\,\text{m s}^{-1}$, $v_{\text{storm}} = 1\,\text{m s}^{-1}$. Only hail with final sizes > 1.5 cm are shown. The maximum hail size[10] to fall in each 200 m $\times$ 200 m pixel is displayed in Fig. 27a, and the number of hailstones > 1.5 cm to fall in each pixel is shown in Fig. 27b. Clearly, both maximum size and number concentration vary substantially both along and across the hail swath. Given adequate computational resources, it is feasible to simulate such hail swaths in an operational setting, prior to convection initiation, initialized with observed or model-forecast soundings. This could be done offline, as shown here, or within operational numerical weather prediction models, similar to Adams-Selin and Ziegler (2016).

[10] The somewhat jagged appearance in places is a result of using discrete (60-s) time steps, much like radar-based swath products.

Brought to you by Pennsylvania State University, Paterno Library | Unauthenticated | Downloaded 10/11/21 01:54 PM UTC

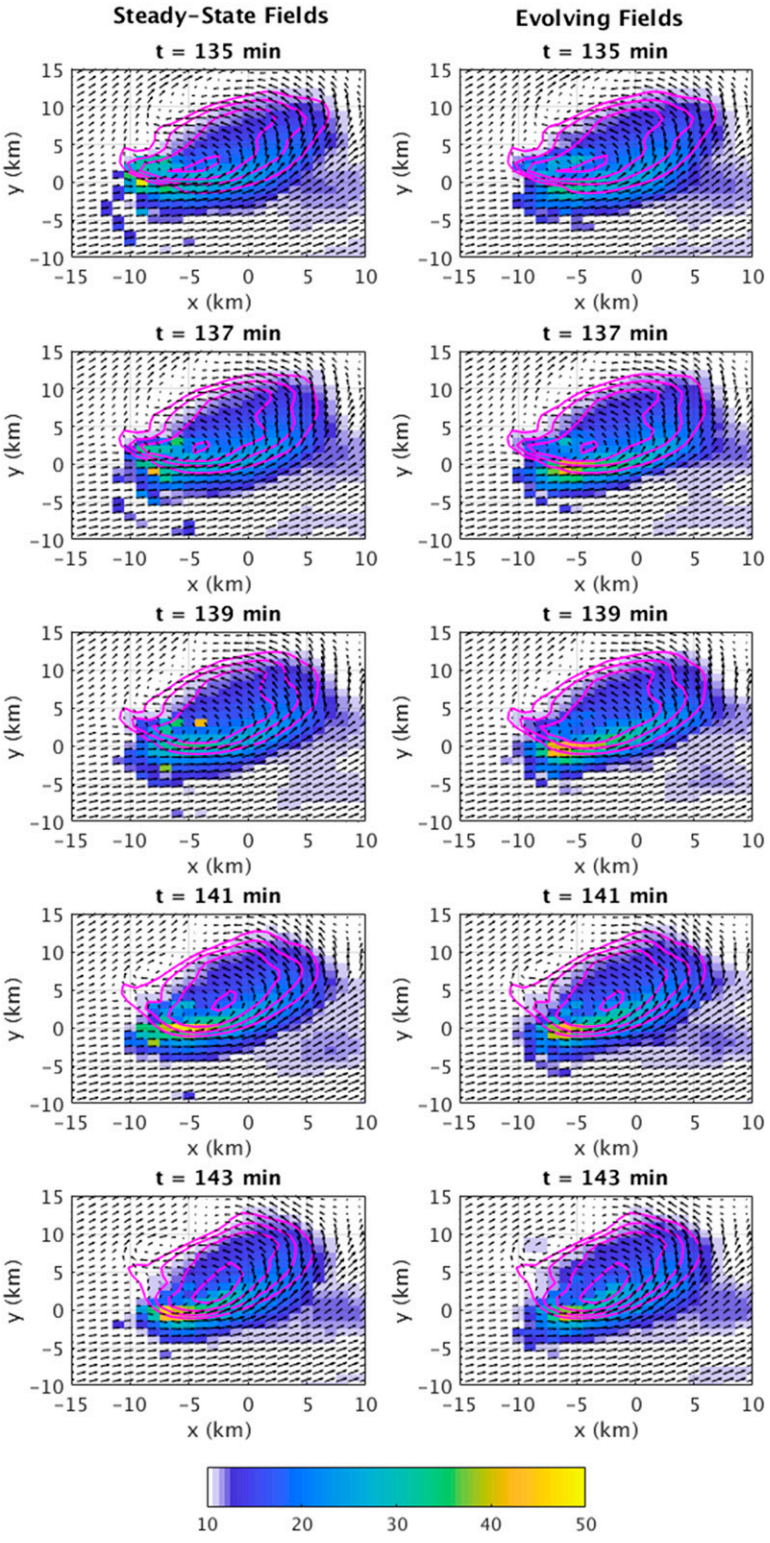

FIG. 26. Comparison of 5.75-km AGL embryo source maps, colored by final hail size (mm, shaded according to color bar at the bottom of the plot) attained by embryos starting at that location, for the (left) steady-state fields and (right) evolving fields. Magenta contours are the 10, 20, 30, 40, and 50 m s^{-1} updraft; black vectors are the horizontal storm-relative winds at this height.

Brought to you by Pennsylvania State University, Paterno Library | Unauthenticated | Downloaded 10/11/21 01:54 PM UTC

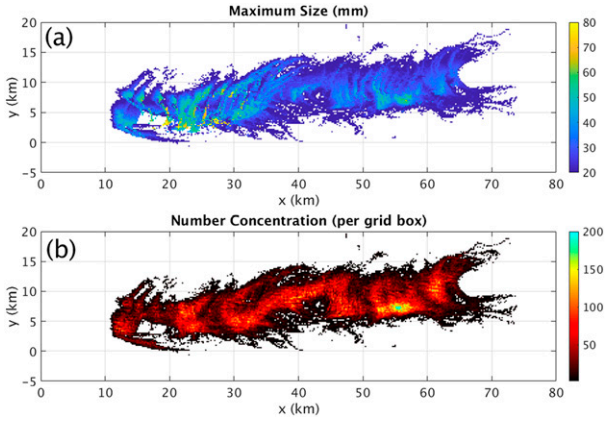

FIG. 27. Simulated hail swath showing (a) maximum sizes (in mm, shaded according to outset color bar) and (b) number concentration of hailstones ≥ 1.5 cm in diameter (per grid box, shaded according to outset color bar), from the umax41-El Reno storm for the 1-h period. Hailstone fallout locations are mapped onto a grid with 200 m × 200 m spacing.

The comparatively sparse and biased nature of hail reports (e.g., see Allen and Tippett 2015) would suggest inadequate sampling of such a hail swath, particularly of the "true" storm maximum hail size. Thus, *any attempts to correlate environmental parameters or other favorable conditions to hail sizes will almost certainly suffer from this type of sampling issue, likely obfuscating any underlying or true relationships* (if they exist). Though our simulations are highly idealized, they do point to the critical need to characterize hail properties along and across the hail swath, not just at point locations, as is typical from hail reports. Such observations, likely only available from a dedicated field campaign or similar concerted effort (e.g., Ortega et al. 2009) when coupled with radar observations, should help provide support or refute the findings herein. Some new technologies, including drone aerial photogrammetry (e.g., Soderholm et al. 2020), may facilitate obtaining such observations.

Our study is limited by considering only a few illustrative cases. For example, only two different thermodynamic environments were tested. Work to systematically explore the influence of CAPE on hail production (through changes in updraft speed, breadth, and horizontal flow patterns) is underway (Lin and Kumjian 2021, manuscript submitted to *J. Atmos. Sci.*). Additional experiments with more realistic hodographs, spanning a larger range of the observed hailstorm environmental parameter space than our previous work (DK17; KL2020), are also planned. Environmental heterogeneities also clearly can play a role in modulating hail production in storms; there is a clear need to better understand these, too. Ultimately, this line of inquiry should improve our understanding and anticipation of the evolving hail risk in severe storms.

Acknowledgments. Funding for this work is from the National Science Foundation Grants AGS-1661679 and AGS-1855063, as well as an award from the Insurance Institute for Business and Home Safety (IBHS). We are also grateful for discussions with Yuzhu Lin (PSU), Ian Giammanco (IBHS), Charlie Knight (NCAR), Rebecca Adams-Selin (AER), Conrad Ziegler (NSSL), and John Allen (CMU). The excellent and constructive reviews from the three anonymous reviewers significantly improved the quality and clarity of this manuscript. Finally, the authors thank Dr. George Bryan for his continued development and improvements of CM1.

Data availability statement. The source code for CM1 is freely available from NCAR, and include some of the base-state environments used in this study. The El Reno environment is available online at http://orf.media/wp-content/uploads/2018/01/elreno2011-05-24-sounding.txt. The hail trajectory code is available from the first author.

REFERENCES

Adams-Selin, R., and C. L. Ziegler, 2016: Forecasting hail using a one-dimensional hail growth model within WRF. *Mon. Wea. Rev.*, **144**, 4919–4939, https://doi.org/10.1175/MWR-D-16-0027.1.

Adlerman, E. J., and R. P. Davies-Jones, 1999: A numerical simulation of cyclic mesocyclogenesis. *J. Atmos. Sci.*, **56**, 2045–2069, https://doi.org/10.1175/1520-0469(1999)056<2045:ANSOCM>2.0.CO;2.

——, and K. K. Droegemeier, 2002: The sensitivity of numerically simulated cyclic mesocyclogenesis to variations in model physical and computational parameters. *Mon. Wea. Rev.*, **130**, 2671–2691, https://doi.org/10.1175/1520-0493(2002)130<2671:TSONSC>2.0.CO;2.

——, and ——, 2005: The dependence of numerically simulated cyclic mesocyclogenesis upon environmental vertical wind shear. *Mon. Wea. Rev.*, **133**, 3595–3623, https://doi.org/10.1175/MWR3039.1.

Allen, J. T., and M. K. Tippett, 2015: The characteristics of United States hail reports: 1955–2014. *Electron. J. Severe Storms Meteor.*, **10** (3), https://www.ejssm.org/ojs/index.php/ejssm/article/view/149.

——, I. M. Giammanco, M. R. Kumjian, H. J. Punge, Q. Zhang, P. Groenemeijer, M. Kunz, and K. Ortega, 2020: Understanding hail in the Earth system. *Rev. Geophys.*, **58**, e2019RG000665, https://doi.org/10.1029/2019RG000665.

Aydin, K., T. A. Seliga, and V. Balaji, 1986: Remote sensing of hail with a dual linear polarized radar. *J. Climate Appl. Meteor.*, **25**, 1475–1484, https://doi.org/10.1175/1520-0450(1986)025<1475:RSOHWA>2.0.CO;2.

Beck, J. R., J. L. Schroeder, and J. M. Wurman, 2006: High-resolution dual-Doppler analyses of the 29 May 2001 Kress, Texas, cyclic supercell. *Mon. Wea. Rev.*, **134**, 3125–3148, https://doi.org/10.1175/MWR3246.1.

Blair, S. F., D. R. Deroche, J. M. Boustead, J. W. Leighton, B. L. Barjenbruch, and W. P. Gargan, 2011: A radar-based assessment of the detectability of giant hail. *Electron. J. Severe Storms Meteor.*, **6** (7), https://www.ejssm.org/ojs/index.php/ejssm/article/viewArticle/87.

——, and Coauthors, 2017: High-resolution hail observations: Implications for NWS warning operations. *Wea. Forecasting*, **32**, 1101–1119, https://doi.org/10.1175/WAF-D-16-0203.1.

Brook, J. P., A. Protat, J. Soderholm, J. T. Carlin, H. McGowan, and R. A. Warren, 2021: HailTrack—Improving radar-based hailfall estimates by modeling hail trajectories. *J. Appl. Meteor. Climatol.*, **60**, 237–254, https://doi.org/10.1175/JAMC-D-20-0087.1.

Brown, T. M., W. H. Pogorzelski, and I. M. Giammanco, 2015: Evaluating hail damage using property insurance claims data.

Brought to you by Pennsylvania State University, Paterno Library | Unauthenticated | Downloaded 10/11/21 01:54 PM UTC

Wea. Climate Soc., **7**, 197–210, https://doi.org/10.1175/WCAS-D-15-0011.1.

Browning, K. A., and G. B. Foote, 1976: Air-flow and hail growth in supercell storms and some implications for hail suppression. *Quart. J. Roy. Meteor. Soc.*, **102**, 499–533, https://doi.org/10.1002/qj.49710243303.

Bryan, G. H., and J. M. Fritsch, 2002: A benchmark simulation for moist nonhydrostatic numerical models. *Mon. Wea. Rev.*, **130**, 2917–2928, https://doi.org/10.1175/1520-0493(2002)130<2917:ABSFMN>2.0.CO;2.

Bunkers, M. J., B. A. Klimowski, J. W. Zeitler, R. L. Thompson, and M. L. Weisman, 2000: Predicting supercell motion using a new hodograph technique. *Wea. Forecasting*, **15**, 61–79, https://doi.org/10.1175/1520-0434(2000)015<0061:PSMUAN>2.0.CO;2.

Changnon, S., D. Changnon, and S. D. Hilberg, 2009: Hailstorms across the nation: An atlas about hail and its damages. Illinois State Water Survey Contract Rep. 2009-12, 92 pp.

Coffer, B. E., and M. Parker, 2017: Simulated supercells in non-tornadic and tornadic VORTEX2 environments. *Mon. Wea. Rev.*, **145**, 149–180, https://doi.org/10.1175/MWR-D-16-0226.1.

Dahl, J., 2017: Tilting of horizontal shear vorticity and the development of updraft rotation in supercell thunderstorms. *J. Atmos. Sci.*, **74**, 2997–3020, https://doi.org/10.1175/JAS-D-17-0091.1.

Davies-Jones, R., 1984: Streamwise vorticity: The origin of updraft rotation in supercell storms. *J. Atmos. Sci.*, **41**, 2991–3006, https://doi.org/10.1175/1520-0469(1984)041<2991:SVTOOU>2.0.CO;2.

——, R. J. Trapp, and H. B. Bluestein, 2001: Tornadoes and tornadic storms. *Severe Convective Storms*, *Meteor. Monogr.*, No. 28, Amer. Meteor. Soc., 167–221, https://doi.org/10.1175/0065-9401-28.50.167.

Deardorff, J. W., 1980: Stratocumulus-capped mixed layers derived from a three-dimensional model. *Bound.-Layer Meteor.*, **18**, 495–527, https://doi.org/10.1007/BF00119502.

Dennis, E. J., and M. R. Kumjian, 2017: The impact of vertical wind shear on hail growth in simulated supercells. *J. Atmos. Sci.*, **74**, 641–663, https://doi.org/10.1175/JAS-D-16-0066.1.

Depue, T. K., P. C. Kennedy, and S. A. Rutledge, 2007: Performance of the hail differential reflectivity (H_{DR}) polarimetric radar hail indicator. *J. Appl. Meteor.*, **46**, 1290–1301, https://doi.org/10.1175/JAM2529.1.

Efron, B., and R. J. Tibshirani, 1993: *An Introduction to the Bootstrap*. 1st ed. Chapman and Hall, 456 pp.

French, M. M., H. B. Bluestein, D. C. Dowell, L. J. Wicker, M. R. Kramar, and A. L. Pazmany, 2008: High-resolution, mobile Doppler radar observations of cyclic mesocyclogenesis in a supercell. *Mon. Wea. Rev.*, **136**, 4997–5016, https://doi.org/10.1175/2008MWR2407.1.

——, ——, I. PopStefanija, C. A. Baldi, and R. T. Bluth, 2013: Reexamining the vertical development of tornadic vortex signatures in supercells. *Mon. Wea. Rev.*, **141**, 4576–4601, https://doi.org/10.1175/MWR-D-12-00315.1.

——, D. W. Burgess, E. R. Mansell, and L. J. Wicker, 2015: Hook echo raindrop sizes retrieved using mobile, polarimetric Doppler radar observations. *J. Appl. Meteor. Climatol.*, **54**, 423–450, https://doi.org/10.1175/JAMC-D-14-0171.1.

Grant, L. D., and S. C. van den Heever, 2014: Microphysical and dynamical characteristics of low-precipitation and classic supercells. *J. Atmos. Sci.*, **71**, 2604–2624, https://doi.org/10.1175/JAS-D-13-0261.1.

Grieser, J., and M. Hill, 2019: How to express hail intensity—Modeling the hailstone size distribution. *J. Appl. Meteor. Climatol.*, **58**, 2329–2345, https://doi.org/10.1175/JAMC-D-18-0334.1.

Gutierrez, R. E., and M. R. Kumjian, 2021: Environmental and radar characteristics of gargantuan hail-producing storms. *Mon. Wea. Rev.*, **149**, 2523–2538, https://doi.org/10.1175/MWR-D-20-0298.1.

Heymsfield, A. J., 1983: Case study of a hailstorm in Colorado. Part IV: Graupel and hail growth mechanisms deduced through particle trajectory calculations. *J. Atmos. Sci.*, **40**, 1482–1509, https://doi.org/10.1175/1520-0469(1983)040<1482:CSOAHI>2.0.CO;2.

Katona, B., and P. Markowski, 2021: Assessing the influence of complex terrain on severe convective environments in northeastern Alabama. *Wea. Forecasting*, **36**, 1003–1029, https://doi.org/10.1175/WAF-D-20-0136.1.

——, ——, C. Alexander, and S. Benjamin, 2016: The influence of topography on convective storm environments in the eastern United States as deduced from the HRRR. *Wea. Forecasting*, **31**, 1481–1490, https://doi.org/10.1175/WAF-D-16-0038.1.

Klemp, J. B., and R. Wilhelmson, 1978: The simulation of three-dimensional convective storm dynamics. *J. Atmos. Sci.*, **35**, 1070–1096, https://doi.org/10.1175/1520-0469(1978)035<1070:TSOTDC>2.0.CO;2.

Knight, N. C., 1981: The climatology of hail embryos. *J. Appl. Meteor.*, **20**, 750–755, https://doi.org/10.1175/1520-0450(1981)020<0750:TCOHE>2.0.CO;2.

Kumjian, M. R., and A. V. Ryzhkov, 2008: Polarimetric signatures in supercell thunderstorms. *J. Appl. Meteor. Climatol.*, **47**, 1940–1961, https://doi.org/10.1175/2007JAMC1874.1.

——, and K. Lombardo, 2020: A hail growth trajectory model for exploring the environmental controls on hail size: Model physics and idealized tests. *J. Atmos. Sci.*, **77**, 2765–2791, https://doi.org/10.1175/JAS-D-20-0016.1.

——, A. V. Ryzhkov, V. M. Melnikov, and T. J. Schuur, 2010: Rapid-scan super-resolution observations of a cyclic supercell with a dual-polarization WSR-88D. *Mon. Wea. Rev.*, **138**, 3762–3786, https://doi.org/10.1175/2010MWR3322.1.

——, and Coauthors, 2020: Gargantuan hail in Argentina. *Bull. Amer. Meteor. Soc.*, **101**, E1241–E1258, https://doi.org/10.1175/BAMS-D-19-0012.1.

Lebo, Z. J., and H. C. Morrison, 2015: Effects of horizontal and vertical grid spacing on mixing in simulated squall lines and implications for convective strength and structure. *Mon. Wea. Rev.*, **143**, 4355–4375, https://doi.org/10.1175/MWR-D-15-0154.1.

Letkewicz, C. E., and M. D. Parker, 2011: Impact of environmental variations on simulated squall lines interacting with terrain. *Mon. Wea. Rev.*, **139**, 3163–3183, https://doi.org/10.1175/2011MWR3635.1.

Lombardo, K. A., 2020: Squall line response to coastal mid-Atlantic thermodynamic heterogeneities. *J. Atmos. Sci.*, **77**, 4143–4170, https://doi.org/10.1175/JAS-D-20-0044.1.

——, and T. Kading, 2018: The behavior of squall lines in horizontally heterogeneous coastal environments. *J. Atmos. Sci.*, **75**, 1243–1269, https://doi.org/10.1175/JAS-D-17-0248.1.

Markowski, P. M., 2020: What is the intrinsic predictability of tornadic supercell thunderstorms? *Mon. Wea. Rev.*, **148**, 3157–3180, https://doi.org/10.1175/MWR-D-20-0076.1.

——, and Y. P. Richardson, 2010: *Mesoscale Meteorology in Midlatitudes*. 1st ed. Wiley-Blackwell, 407 pp.

——, and N. Dotzek, 2011: A numerical study of the effects of orography on supercells. *Atmos. Res.*, **100**, 457–478, https://doi.org/10.1016/j.atmosres.2010.12.027.

——, and Y. P. Richardson, 2014: The influence of environmental low-level shear and cold pools on tornadogenesis: Insights from idealized simulations. *J. Atmos. Sci.*, **71**, 243–275, https://doi.org/10.1175/JAS-D-13-0159.1.

Brought to you by Pennsylvania State University, Paterno Library | Unauthenticated | Downloaded 10/11/21 01:54 PM UTC

Miller, L. J., J. D. Tuttle, and C. A. Knight, 1988: Airflow and hail growth in a severe northern plains supercell. *J. Atmos. Sci.*, **45**, 736–762, https://doi.org/10.1175/1520-0469(1988)045<0736:AAHGIA>2.0.CO;2.

Morgan, G. M., and N. G. Towery, 1975: Small-scale variability of hail and its significance for hail prevention experiments. *J. Appl. Meteor.*, **14**, 763–770, https://doi.org/10.1175/1520-0450(1975)014<0763:SSVOHA>2.0.CO;2.

Morrison, H., 2016: Impacts of updraft size and dimensionality on the perturbation pressure and vertical velocity in cumulus convection: Part I: Simple, generalized analytic solutions. *J. Atmos. Sci.*, **73**, 1441–1454, https://doi.org/10.1175/JAS-D-15-0040.1.

——, G. Thompson, and V. Tatarskii, 2009: Impact of cloud microphysics on the development of trailing stratiform precipitation in a simulated squall line: Comparison of one- and two-moment schemes. *Mon. Wea. Rev.*, **137**, 991–1007, https://doi.org/10.1175/2008MWR2556.1.

Mulholland, J. P., S. W. Nesbitt, R. J. Trapp, and J. M. Peters, 2020: The influence of terrain on the convective environment and associated convective morphology from an idealized modeling prospective. *J. Atmos. Sci.*, **77**, 3929–3949, https://doi.org/10.1175/JAS-D-19-0190.1.

Murillo, E. M., and C. R. Homeyer, 2019: Severe hail fall and hailstorm detection using remote sensing observations. *J. Appl. Meteor. Climatol.*, **58**, 947–970, https://doi.org/10.1175/JAMC-D-18-0247.1.

National Weather Service, 2016: Weather event summary: San Antonio April 2016. NWS Rep., 5 pp., https://www.weather.gov/media/ewx/wxevents/ewx-20160412.pdf.

Nelson, S. P., 1983: The influence of storm flow structure on hail growth. *J. Atmos. Sci.*, **40**, 1965–1983, https://doi.org/10.1175/1520-0469(1983)040<1965:TIOSFS>2.0.CO;2.

Orf, L., R. Wilhelmoson, B. Lee, C. Finley, and A. Houston, 2017: Evolution of a long-track violent tornado within a simulated supercell. *Bull. Amer. Meteor. Soc.*, **98**, 45–68, https://doi.org/10.1175/BAMS-D-15-00073.1.

Ortega, K. L., T. M. Smith, K. L. Manross, A. G. Kolodziej, K. A. Scharfenberg, A. Witt, and J. J. Gourley, 2009: The Severe Hazards Analysis and Verification Experiment. *Bull. Amer. Meteor. Soc.*, **90**, 1519–1530, https://doi.org/10.1175/2009BAMS2815.1.

——, J. M. Krause, and A. V. Ryzhkov, 2016: Polarimetric radar characteristics of melting hail. Part III: Validation of the algorithm for hail size discrimination. *J. Appl. Meteor. Climatol.*, **55**, 829–848, https://doi.org/10.1175/JAMC-D-15-0203.1.

Peters, J. M., C. J. Nowotarski, and H. C. Morrison, 2019: The role of vertical wind shear in modulating maximum supercell updraft velocities. *J. Atmos. Sci.*, **76**, 3169–3189, https://doi.org/10.1175/JAS-D-19-0096.1.

——, ——, J. P. Mulholland, and R. L. Thompson, 2020: The influences of effective inflow layer streamwise vorticity and storm-relative flow on supercell updraft properties. *J. Atmos. Sci.*, **77**, 3033–3057, https://doi.org/10.1175/JAS-D-19-0355.1.

Púčik, T., C. Castellano, P. Groenemeijer, T. Kühne, A. T. Rädler, B. Antonescu, and E. Faust, 2019: Large hail incidence and its economic and societal impacts across Europe. *Mon. Wea. Rev.*, **147**, 3901–3916, https://doi.org/10.1175/MWR-D-19-0204.1.

Punge, H. J., and M. Kunz, 2016: Hail observations and hailstorm characteristics in Europe: A review. *Atmos. Res.*, **176–177**, 159–184, https://doi.org/10.1016/j.atmosres.2016.02.012.

Rasmussen, R. M., and A. J. Heymsfield, 1987: Melting and shedding of graupel and hail. Part III: Investigation of the role of shed drops as hail embryos in the 1 August CCOPE severe storm. *J. Atmos. Sci.*, **44**, 2783–2803, https://doi.org/10.1175/1520-0469(1987)044<2783:MASOGA>2.0.CO;2.

Richardson, Y. P., K. K. Droegemeier, and R. P. Davies-Jones, 2007: The influence of horizontal environmental variability on numerically simulated convective storms. Part I: Variations in vertical shear. *Mon. Wea. Rev.*, **135**, 3429–3455, https://doi.org/10.1175/MWR3463.1.

Ryzhkov, A. V., M. R. Kumjian, S. M. Ganson, and P. Zhang, 2013: Polarimetric radar characteristics of melting hail. Part II: Practical implications. *J. Appl. Meteor. Climatol.*, **52**, 2871–2886, https://doi.org/10.1175/JAMC-D-13-074.1.

Soderholm, J., H. McGowan, H. Richter, K. Walsh, T. Weckwerth, and M. Coleman, 2017: An 18-year climatology of hailstorm trends and related drivers across southeast Queensland, Australia. *Quart. J. Roy. Meteor. Soc.*, **143**, 1123–1135, https://doi.org/10.1002/qj.2995.

——, M. R. Kumjian, N. McCarthy, P. Maldonado, and M. Wang, 2020: Quantifying hail size distributions from the sky—Application of drone aerial photogrammetry. *Atmos. Meas. Tech.*, **13**, 747–754, https://doi.org/10.5194/amt-13-747-2020.

Tessendorf, S. A., L. J. Miller, K. C. Wiens, and S. A. Rutledge, 2005: The 29 June supercell observed during STEPS. Part I: Kinematics and microphysics. *J. Atmos. Sci.*, **62**, 4127–4150, https://doi.org/10.1175/JAS3585.1.

Trapp, R. J., G. R. Marion, and S. W. Nesbitt, 2017: The regulation of tornado intensity by updraft width. *J. Atmos. Sci.*, **74**, 4199–4211, https://doi.org/10.1175/JAS-D-16-0331.1.

Warren, R. A., H. Richter, H. A. Ramsay, S. T. Siems, and M. J. Manton, 2017: Impact of variations in upper-level shear on simulated supercells. *Mon. Wea. Rev.*, **145**, 2659–2681, https://doi.org/10.1175/MWR-D-16-0412.1.

Weisman, M. L., and J. B. Klemp, 1984: The structure and classification of numerically simulated convective storms in directionally varying wind shears. *Mon. Wea. Rev.*, **112**, 2479–2498, https://doi.org/10.1175/1520-0493(1984)112<2479:TSACON>2.0.CO;2.

——, and R. Rotunno, 2000: The use of vertical wind shear versus helicity in interpreting supercell dynamics. *J. Atmos. Sci.*, **57**, 1452–1472, https://doi.org/10.1175/1520-0469(2000)057<1452:TUOVWS>2.0.CO;2.

Witt, A., and J. C. Snyder, 2018: WSR-88D observations of an extreme hail event impacting western South Dakota on 20 June 2015. *29th Conf. on Severe Local Storms*, Stowe, VT, Amer. Meteor. Soc., 9, https://ams.confex.com/ams/29SLS/webprogram/Paper348276.html.

——, N. D. Eilts, G. J. Stumpf, J. T. Johnson, E. D. Mitchell, and K. W. Thomas, 1998: An enhanced hail detection algorithm for the WSR-88D. *Wea. Forecasting*, **13**, 286–303, https://doi.org/10.1175/1520-0434(1998)013<0286:AEHDAF>2.0.CO;2.

——, D. W. Burgess, A. Seimon, J. T. Allen, J. C. Snyder, and H. B. Bluestein, 2018: Rapid-scan radar observations of an Oklahoma tornadic hailstorm producing giant hail. *Wea. Forecasting*, **33**, 1263–1282, https://doi.org/10.1175/WAF-D-18-0003.1.

Ziegler, C. L., P. S. Ray, and N. C. Knight, 1983: Hail growth in an Oklahoma multicell storm. *J. Atmos. Sci.*, **40**, 1768–1791, https://doi.org/10.1175/1520-0469(1983)040<1768:HGIAOM>2.0.CO;2.

Brought to you by Pennsylvania State University, Paterno Library | Unauthenticated | Downloaded 10/11/21 01:54 PM UTC